Computational studies of strongly correlated quantum magnets

A thesis submitted to
Tata Institute of Fundamental Research, Mumbai
for the degree of Doctor of Philosophy
in Physics

by

Argha Banerjee
Department of Theoretical Physics
Tata Institute of Fundamental Research
Mumbai

November 2010

Acknowledgements

I would like to acknowledge the guidance received from my thesis advisor Kedar Damle. I am deeply grateful to all my colleagues and teachers for their invaluable help. Finally, I would like to thank my family members and friends for their support and encouragement.

Declaration

This thesis is a presentation of my original research work. Wherever contributions of others are involved, every effort is made to indicate this clearly, with due reference to the literature, and acknowledgement of collaborative research and discussions.

The work was done under the guidance of Kedar Damle, at the Tata Institute of Fundamental Research, Mumbai.

Candidate: ..... Date: .....
(Argha Banerjee)

In my capacity as supervisor of the candidate's thesis, I certify that the above statements are true to the best of my knowledge.

Thesis advisor: ..... Date: .....
(Kedar Damle)

Contents

1

Introduction

In condensed matter physics, we understand various physical systems through careful experiments, and explain the experimentally observed behaviour of the real materials with the help of simple models. Inputs from the experiments help refine the models, and better understanding of the models in turn leads to sharper experimental questions. Experiments typically study the response of the system to the changes in various control parameters and interactions of the system with different physical probes. A successful model for the system under study must take into account the relevant microscopic degrees of freedom and their interactions - so that it can be used to obtain precise quantitative results which compares well with the experimental measurements. The model must be able to provide answers to the detailed questions regarding the physical properties of the system in the particular experimental set-up, and simultaneously be general enough to give insight into similar phenomena taking place in other physical systems.

In the presence of complex interactions among macroscopically large number of degrees of freedom in an exponentially large Hilbert space, exact analytic calculations of relevant physical properties of the model system are often too difficult to achieve. In fact, even with the simplest of interactions most of the the many body problems elude exact solution. The situation becomes more difficult at two or three spatial dimensions. To get around these difficulties various approximation schemes are used extensively. For example, using various perturbative techniques, the effect of relatively weak additional interactions on a solvable system can be taken into account in a systematic series of controlled corrections. Sometimes the full model with all its interactions can be simplified into an effective model that works well at the energy scales relevant to the experiments. Apart from such analytic approaches, another powerful and

routinely employed tool is computer simulations. With exponentially increasing computing power of modern machines, simulations allow us to access various physical properties of complex systems with large number of degrees of freedom. Numerical methods are extremely useful in calculating the detailed properties of a particular system and its response to various experimental probes. They are also widely used to solve various models to check and validate the results of approximate analytical schemes.

In this chapter, we first discuss an example of how a model describing electron hopping around on a lattice can be reduced to that of spin moments localised on lattice sites, with Heisenberg interactions between them. Then, we review some of the numerical tools that are used to study spin systems. These discussions serve as the background for this thesis on numerical study of ground state properties of quantum spin systems.

1.1 Heisenberg spin model

The most elementary microscopic model to describe electrons in a solid is the tight-binding model[AM03]. The solid atoms are approximated by a frozen periodic potential and non-interacting electrons occupy localised wavefunctions centered at each lattice site. The small overlaps between localised orbitals at near-neighbour sites allow electron tunnelling, so that the the Hamiltonian looks like,

$$H = -t \sum_{\langle ij\rangle\sigma} (c_{i,\sigma} c^{\dagger}_{j,\sigma} + h.c.) + \mu \sum_{i\sigma} n_{i\sigma}. \tag{1.1}$$

Here t is the strength of hopping, $c_{i,\sigma}(c^{\dagger}_{i,\sigma})$ is the electron creation (annihilation) operator on the ith lattice site with spin $\sigma = \pm 1/2$, $\langle ij\rangle$ denotes a near neighbour pair of sites, $n_{i\sigma} = c^{\dagger}_{i,\sigma} c_{i,\sigma}$ is the number operator, and the chemical potential μ controls the total electron density.

Although the above model can be solved easily and provide explanations of many material properties with some degree of success, it cannot explain, for example, why certain materials with half-filled conduction bands behaves as insulators, known as "Mott insulators". It turns out that, to remedy this, one must include electron-electron Coulomb repulsion in this model. The simplest way to do that is to approximate the screened Coulomb interaction by a onsite repulsion term: with this mod-

ification the model is known as the Hubbard model[Aue94a],

$$H = \sum_{\langle ij\rangle\sigma} -t(c_{i,\sigma}{c_{j,\sigma}}^{\dagger} + h.c.) + \sum_{i\sigma} U n_{i,\uparrow} n_{i,\downarrow} + \mu \sum_{i\sigma} n_{i\sigma}. \tag{1.2}$$

Even with this apparently simple-minded treatment of electron-electron interactions, the Hubbard model contains rich physics, and is studied extensively to understand complex phenomena like metal-insulator transition [IFT98], high temperature superconductivity[Dag94] and so on. But unfortunately, this model cannot be solved exactly in more than one dimensions. An approximate approach to extract useful information out of this model is to look at the limiting case of $U/t \gg 1$, which holds true in many experimental examples of Mott insulators, for instance the parent compounds of the high-T_c superconductors. In this limit, the model reduces to that of static spin-1/2 moments interacting with each other by nearest-neighbour Heisenberg exchange interaction. This model is known as the Heisenberg model,

$$H = J \sum_{\langle ij\rangle} \mathbf{S}_i \cdot \mathbf{S}_j, \tag{1.3}$$

where $\mathbf{S}_i$ is the $S = 1/2$ spin moment at site i and $\langle ij\rangle$ denotes a near neighbour pair of sites.

This effective spin model describing the low energy physics of the Hubbard model is obtained by considering the effect of the small perturbative t term on the infinite-U ground state manifold, where the qualifier "low energy" implies energies much lower than U. At infinite U/t, that is $t = 0$, the electrons cannot hop anymore and the ground state manifold at half-filling is given by the set of states with one electron at each site with arbitrary spin orientations. Now, turning on a small but finite t would allow electrons to hop. But a single hop creates a state with a doubly occupied site, and due to an associated energy cost of $\sim U$ takes it out of the ground state manifold. But in the next order in perturbation theory, the ground state energy can be lowered by going up to an excited state with a doubly occupied site and coming down again by a hop back to the empty site. This second order process lowers the ground state energy by an amount $\sim t^2/U$. If near-neighbour sites are occupied by electrons with same spin-states, then Pauli exclusion principle prevents the double occupancy of a site and the virtual hop is not allowed anymore. Thus, a pair of near-neighbour sites can lower energy by $\sim t^2/U$, only if they

are occupied by spins with opposite polarisations - this leads to the effective Heisenberg interaction(1.3) between spin moments which favours opposite spin orientations of all the near neighbour pairs.

The Heisenberg spin model is used successfully to explain various experimental properties of numerous physical systems. For example, the parent compounds of the high T_c superconductors, the cuprates, contain copper oxide planes where spin-moments on Cu atoms are well described by a $S = 1/2$ Heisenberg model on a square lattice[Man91]. But unfortunately, despite its apparently simple structure, non-trivial commutation relations of the spin operators make it hard to solve. This model cannot be handled analytically in more than one dimension, unless one settles for various approximate analytical schemes like spin-wave theory[Aue94b]. That is why various numerical methods are very important to extract observable prediction out of this model. For example, there is no rigorous proof of the existence of antiferromagnetic long range order in the the ground of $S = 1/2$ Heisenberg model on a square lattice. Only through quantum Monte Carlo simulations[RY88], was the presence of such an ordering shown beyond doubt.

In this thesis, we have mostly dealt with the $S = 1/2$ Heisenberg model or certain variants of it. The $S = 1/2$ Heisenberg model has been studied extensively in literature in various theoretical and experimental contexts, using all kinds of sophisticated analytical and numerical tools. In spite of that, some new and intriguing results were found in our numerical investigations of this model on the square lattice with open boundaries. In our study of models where the Heisenberg interactions compete with certain multispin interactions favouring a class of lattice symmetry broken states, we have established the presence of phase transitions from Néel ordered phase to bond ordered solid phase. These transitions can either be continuous or first order, depending on the geometry of the additional multi-spin interactions. When the transitions are continuous, they are counter examples to the standard Landau theory of phase transitions, and must be understood in terms of so called deconfined critical phenomena. Our numerical work, involving study impurity effects at these continuous transition, provides evidence for the continuous nature of some of these transitions, and also raises important questions that must be answered by the theories striving to describe this class of phase transitions: In particular, our finding of logarithmic violations of scaling at these deconfined critical points suggests that a reexamination of the field theory for these unusual critical points.

1.2 Numerical tools to study spin systems

As discussed in the previous section, the use of powerful numerical tools is indispensable to the study of even the simplest of the spin systems like the Heisenberg model. Thus, it is very important for condensed matter physicists to try to invent new computational techniques and to improve the existing ones. Enormous progress has been made in this direction and as a result many sophisticated numerical tools have come up. Application of these sophisticated techniques allow a wide range of physical observables to be computed to great accuracy - and that too, for systems consisting of thousands of interacting spins. In the following sections, we discuss some of these important numerical techniques, which are very useful to study properties of various spin systems.

1.2.1 Exact diagonalisation

An obvious method to solve spin models is to numerically diagonalise the Hamiltonian matrix in a convenient basis[Man91]. With full spectrum of energy eigenvalues and corresponding wave-functions available through exact diagonalisation, any observable can be computed to within the numerical accuracy of modern-day computers. The basic problem with this brute-force diagonalisation scheme is that the dimension of the Hamiltonian matrix grows exponentially with the number of spins present. That makes it impossible to use this method for systems with large number spins. This problem can be alleviated to some extent by appealing to various conserved quantities: the trick is to first reduce the the size of the matrix by block diagonalising the Hamiltonian, and then diagonalising each block separately. But still, this method is not suitable to study the thermodynamic properties of various spin models where access to larger system sizes is a must. But exact diagonalisation is still useful to validate other analytical and numerical methods for small systems.

1.2.2 Finite temperature Monte Carlo

In the context of condensed matter physics, Monte Carlo is a probabilistic method to evaluate expectation values of the form,

$$\langle \mathcal{O} \rangle = \frac{\sum_{\{\mathcal{C}\}} W_{\mathcal{C}} \mathcal{O}_{\mathcal{C}}}{\sum_{\{\mathcal{C}\}} W_{\mathcal{C}}}, \tag{1.4}$$

where $\{\mathcal{C}\}$ is a set of configurations, $W_{\mathcal{C}}$ is the weight of a particular configuration $\mathcal{C}$, and $\mathcal{O}_{\mathcal{C}}$ is the expectation value of the observable $\mathcal{O}$ in the configuration $\mathcal{C}$. This method is based on interpreting $W_{\mathcal{C}}$ as a probability distribution, and then stochastically importance sampling the set of configurations according to that distribution. An efficient algorithm to move from one configuration to another, so that the configuration space is sampled with right weights and in an unbiased manner, is the key to any successful Monte Carlo implementation. The rules that are used to update configurations must allow one to reach all allowed configurations, i.e. the Monte Carlo moves must be ergodic. Another important constraint is that the update rules must satisfy detailed balance conditions which guarantees that the equilibrium distribution of the sampled configurations would indeed be $W_{\mathcal{C}}$. It should be noted that being a probabilistic method, Monte Carlo estimates of observables contain statistical errors. But the accuracy can be improved systematically by sampling more and more configurations. What simplifies the setting up of a state-of-the-art Monte Carlo simulation is that open source implementations of many of these techniques are freely available on the internet[AAC+07].

The prescription for calculating finite temperature properties of a quantum system, described by Hamiltonian H, at temperature T, is to evaluate the sum,

$$\langle \mathcal{O} \rangle = \frac{\sum_{\psi} \langle \psi | \mathcal{O} \exp\left(-H/T\right) | \psi \rangle}{\sum_{\psi} \langle \psi | \exp\left(-H/T\right) | \psi \rangle}. \tag{1.5}$$

Clearly, this has the same from as (1.4) and the sum can be evaluated using appropriate Monte Carlo techniques. Indeed, many sophisticated Monte Carlo techniques have been developed which allow efficient simulations of a wide range of spin interactions with few tens of thousands spin moments being present in the system. Many of these techniques, e.g. Stochastic Series Expansion[San99], continuous time worm algorithm[PST98a, PST98b] and so on, come with clever update procedures which allow for non-local updates of the configurations. These updates dramatically reduce the number of Monte Carlo steps required to go from any given configuration to another, such that they are statistically independent. Also, the estimators for the relevant physical observables are cleverly constructed to ensure that reliable results can be obtained with the minimum of computational effort. Different variations of these Monte Carlo methods are available, which work reliably even in the most difficult of situations. For example, in case of critical slowing down near a

continuous transition, parallel tempering scheme[HN96] is often used. In this method, one simulates several copies of the same system at various different temperatures simultaneously, and interchanges the configurations with appropriate rates that satisfy detailed balance. This helps the system to move around in the configuration space freely without getting stuck in local free energy minima.

One of the issues with these finite temperature techniques is that they do not provide direct access to the ground state properties of the model being simulated, although they are ideal for making contacts with $T > 0$ experimental observables. The ground state properties have to be obtained indirectly, by running multiple simulations at successively lower temperatures and extrapolating to $T = 0$. Moreover, the estimated quantities may contain large extrapolation errors, if the nature of the finite temperature corrections is not known advance.

Another well-known problem, that restricts the scope of all Monte Carlo methods, is the so called sign problem[HS00]. This refers to the situation where sign of the weight $W_{\mathcal{C}}$ is not always positive. Of course, in principle we can redefine the probability weights to be the absolute value of $W_{\mathcal{C}}$, but then, to calculate the expectation values one must also measure the average sign ($sgn(\mathcal{C})$) of the configurations:

$$\begin{aligned} \langle \mathcal{O} \rangle &= \frac{\sum_{\{\mathcal{C}\}} |W_{\mathcal{C}}| sgn(\mathcal{C}) \mathcal{O}_{\mathcal{C}}}{\sum_{\{\mathcal{C}\}} |W_{\mathcal{C}}| sgn(\mathcal{C})} \\ &= \frac{\langle sgn\mathcal{O} \rangle_W}{\langle sgn \rangle_W}. \end{aligned} \tag{1.6}$$

Unfortunately, for most of the problems of interest, in which this sign problem crops up, the sign of the weights fluctuates wildly and the error in the estimate of average sign grows exponentially leading to large errors in all measured observables.

1.2.3 Monte Carlo techniques to study the ground state properties

If one is interested in investigating only the ground state properties of a system, then as it was pointed out above, finite temperature Monte Carlo is not the most efficient way of simulating the system. There are a range of Monte Carlo techniques which can be used more effectively to directly access the ground state properties. These methods include

various variational Monte Carlo tools - where a trial state is defined up to a family of unspecified parameters and they are optimised numerically to approximately describe the ground state of the system concerned. On the other hand, methods like projector Monte Carlo are numerically exact - in the sense that the accuracy can be improved systematically with more and more computing resources. In the later chapter of this thesis one such technique, known as projector Monte Carlo in valence bond basis[San05, SE10], will be discussed in greater detail.

1.3 Experiments and Numerics

With all these powerful Monte Carlo techniques at disposal, the next important task is to identify the right physical observables, that can help us gain insight into the physical properties of the system being studied. In this context, it is very useful to take lessons from experiments. In a numerical simulation, it is often straightforward to mimic an experimental situation or to perform a measurement which closely follows an experimental probe. For example, stochastic series expansion Monte Carlo allows one to study systems with no translational invariance, where most of our analytical tools fail. In fact, in real experiments, because of impurities and inhomogeneities present in the samples, translational symmetry is often broken. Moreover, many important examples are known, where impurities are added intentionally, and their effects reveal important clues about the nature of the physical phenomena being studied[ABGH09]. A classic example of this is the nuclear magnetic resonance study of non-magnetic impurities in Heisenberg spin chain material $Y_2BaNiMgO_5$[TSHac99]. In the antiferromagnetic phase each of these impurities induce a alternating spin texture around them. Since spin polarisation of each Ni atom causes hyperfine splitting of the neighbouring ^{89}Y atom, the resultant multiple peaks in the NMR spectra can be used to reconstruct the microscopic spin texture. A similar impurity induced spin texture have been probed numerically in a bilayer spin model[HSS07a] to gain important insights into the continuous transition from an antiferromagnet to a gapped paramagnet seen in this model. Clearly, it is very useful to employ various numerical tools to set up virtual numerical experiments. It is also very important to look for new simulation techniques that help us capture some particular experimental situation which can not be handled by known simulation techniques.

1.4 Aims of this thesis

In this thesis, we generalise this singlet sector valence bond projector Monte Carlo technique to some cases where the ground state lies in the total spin ($S_{total} = 1/2$) sector[BD10], e.g., ground state of a $S = 1/2$ Heisenberg antiferromagnet consisting of odd number of spins. This extension is very useful in modelling many experimental situations, for instance impurity effects in antiferromagnetic parent compounds doped with non-magnetic Zn/Mg atoms [TSHac99, ABGH09], or boundary effects in nanoscale magnets. In the following chapters, we first describe the original singlet sector valence bond projector Monte Carlo algorithm, and then explain our extension of the same to the total spin $S_{total} = 1/2$ sector. Next, we discuss application of this technique to study the effect of finite size and open edges in $S = 1/2$ Heisenberg antiferromagnets. We study this model on an $L \times L$ square lattice with open boundaries, and L odd. We also investigate the scaling of impurity induced spin texture at bulk quantum critical points for various models[BDA10]. In our study of impurity effects in JQ models, which are supposed to show a deconfined quantum critical transition from an antiferromagnet to a valence bond solid state, we identify logarithmic violations to critical scaling. We also study the nature of the transitions in staggered versions of original JQ models and establish the first order nature of antiferromagnet to valence bond solid transitions in these models.

2

Projector Monte Carlo in Valence bond basis

The singlet sector valence bond Monte Carlo algorithm of Sandvik and coworkers [San05, BS06, SE10] provides an efficient way to estimate ground state expectation values of various physically relevant observables for a wide class of $S = 1/2$ spin systems with even number of spins and bipartite interactions. These technique could be used to study the ground state properties of arbitrary bipartite clusters of even number of spin moments, which is important, for example, to understand the magnetic phase transition in the doped $S = 1/2$ Heisenberg antiferromagnet La_2CuO_4 at a critical concentration of nonmagnetic dopant Zn/Mg[VMG+02]. Using simple variations of this Monte Carlo technique, it also possible to study the triplet excitations above the ground states of the relevant spin models.

In this chapter, first we introduce the original singlet sector valence bond Monte Carlo scheme[San05], and then describe an extension of this Monte Carlo technique to handle systems with odd number of spins [BD10], where the doublet ground states lie in the total spin $S_{total} = 1/2$ sector. This extension complements the original singlet sector algorithm very well. For example, using this method one can study the ground state properties of clusters of odd number of spin $S = 1/2$ moments as well. This $S_{total} = 1/2$ algorithm works as efficiently as the original singlet sector algorithm, and various relevant observables can be estimated using statistics of central overlap loops (defined later), as before. The subsequent presentation is based on joint work with Kedar Damle [BD10].

2.1 Original singlet sector algorithm

The basic principle of this projector algorithm[San05], is to start with an arbitrary state and apply the Hamiltonian operator repeatedly, so that the state with the lowest energy eigenvalue is projected out to within numerical accuracy. To do this, an appropriate positive constant is subtracted from the Hamiltonian so that $|E_0| > |E_n|$ for all $m \neq 0$. Then,

$$\begin{aligned}(C-H)^m|s\rangle &= c_0(-E_0)^m\left(|0\rangle + \sum_{n=1} c_n(|E_n|/|E_0|)^m|n\rangle\right) \\ &\approx c_0(-E_0)^m|0\rangle.\end{aligned} \tag{2.1}$$

Of course, this method would work only when the initial trial state $|s\rangle$ has nonvanishing overlap with the ground state.

2.1.1 Hamiltonians and basis

This particular implementation of projector Monte Carlo method[San05], works for any spin Hamiltonian $H = \sum_k -H_k$, such that each H_k is either a singlet projector $P_{ij} = \frac{1}{4} - \mathbf{S}_i \cdot \mathbf{S}_j$, with sites i,j belonging to different sublattices, or product of such bipartite projectors, e.g.

$$H = -J\sum_{\langle ij\rangle} P_{ij} - Q_2 \sum_{\langle ij,kl\rangle} P_{ij}P_{kl} - Q_3 \sum_{\langle ij,kl,mn\rangle} P_{ij}P_{kl}P_{mn} + \cdots, \tag{2.2}$$

with sum over bonds and plaquettes. Note that, with vanishing Q_2 and Q_3 the Hamiltonian reduces to the Heisenberg Hamiltonian. When both J and Q_2 are non zero, it is known as JQ_2 Hamiltonian, and so on.

The evaluation of the ground state expectation value of an observable $\mathcal{O}$, $\langle s|(-H)^m\mathcal{O}(-H)^m|s\rangle / \langle s|(-H)^{2m}|s\rangle$, requires efficient sampling of all possible strings of operators with $2m$ operators (H_k) present,

$$(-H)^m = (\sum_k -H_k)^m = \sum \prod_{k=1}^{k=m}(-H_k) \tag{2.3}$$

The trial state $|s\rangle$ is expressed in the bipartite valence bond basis, which is an overcomplete basis for the total spin singlet sector[BS06]. The action of individual P_{ij} is very simple in this basis: it reconnects a pair of valence bonds with amplitude $1/2$ if site i,j belong to different valence bonds, and leaves them alone if a valence bond between i,j already exists (as shown

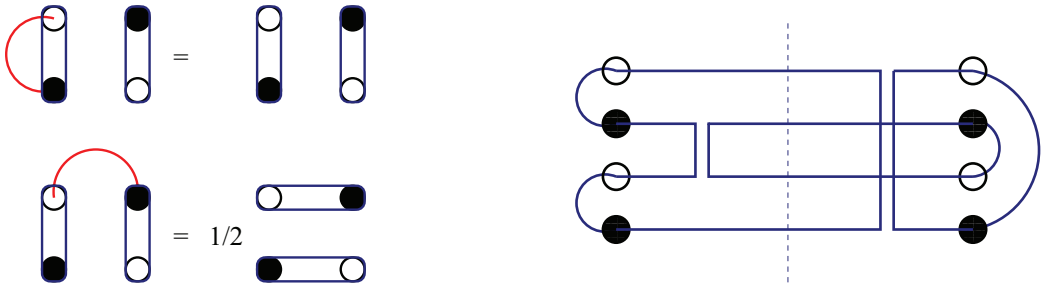

Figure 2.1: Left: The reconnection rules in the valence bond basis. Right: a valence bond Monte Carlo loop configuration for a four site problem with projection length, $m = 1$.

in Fig. 2.1). Taking advantage of these simple rules, the sampling problem is reduced to that of efficiently generating all possible loop configurations, as shown in Fig. 2.1. The efficiency of this method can be improved considerably by using a loop-update method developed by Sandvik and Evertz[SE10] .

2.1.2 Estimators

This algorithm has the added advantage that various observables can be estimated efficiently, using just the statistics of overlap loops of the two valence bond states obtained on the left and right by the action of $(-H)^m$ to the left and and to the right[BS06]. Examples of such loop structures in the overlap of left and right valence bond states are shown in Fig. 2.2 and amplitude of the overlap is simply determined by the number of overlap loops in the graph $(1/2^{N_{loop}})$.Using this simple overlap rules various physical observables can be evaluated. For example, the estimator of expectation value of the operators $\mathbf{S}_i \cdot \mathbf{S}_j$ in the projected ground state is $-\frac{3}{4}$ or 0, depending on whether or not both sites i, j belong to same central valence bond overlap loop. Using this, the estimator for total staggered magnetisation squared can be expressed as[BS06],

$$\langle \mathbf{m}_s^2 \rangle = 3/4 \sum_{\alpha} l_\alpha^2, \tag{2.4}$$

where $\langle \mathbf{m}_s^2 \rangle = \sum_{ij} \epsilon_{ij} \mathbf{S}_i \cdot \mathbf{S}_j$ and index α runs over all central overlap loops of length l_α each. Here, ϵ_{ij} is defined so that it takes the value $+1$ if both

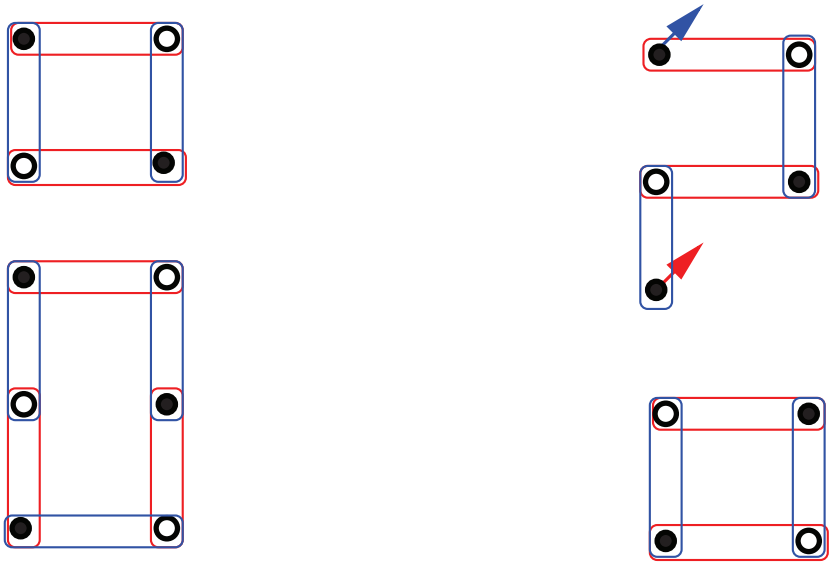

Figure 2.2: The overlap graphs between left (blue) and right (red) singlet sector valence bond basis states contain loops as shown in the left panel. For a graph with N_{loop} number of loops the overlap amplitude is simply $1/2^{N_{loop}}$. The analogous overlap graph for two states in the spin-half valence bond basis will have a single open string joining the two free spins in the left and right valence bond states.

i, j belong to same sublattice, and it equals -1 if they are in different sublattices.

Similarly the estimators for the higher moments of the staggered magnetisation can also be expressed only as functions of statistics of length distribution of central overlap loops in valence bond basis[BS06]. For example,

$$\langle \mathbf{m}_s^4 \rangle = \sum_\alpha \left(-\frac{5}{8} L_\alpha^4 + L_\alpha^2 \right) + 15/16 \left(\sum_\alpha L_\alpha^2 \right)^2 . \tag{2.5}$$

2.2 Generalisation to total spin $S_{total} = 1/2$ sector

Clearly, above singlet sector valence bond projector Monte Carlo technique does not work for systems with odd number of spins, for example, a system where the number of B-sublattice spins (N_B) is one less than

number of A-sublattice spins($N_A = N_B + 1$). In such situations there is a doublet of ground states belonging to $S_{total} = 1/2$ sector. Below we present a generalisation of the original singlet sector algorithm which works equally well in this total spin half sector[BD10]. This extension allows the application of valence bond Monte Carlo to a much wider class of problems e.g. the effect of a single nonmagnetic impurity on the ground state of a magnetic system, ground state properties of arbitrary bipartite clusters with odd number of spins and so on.

2.2.1 Basis

As we have already seen, the algorithm of the singlet sector valence bond Monte Carlo depends crucially on the choice of basis set, which simplifies the matrix elements of each term in the Hamiltonian. Therefore, we need a convenient basis for the $S_{total} = 1/2$ sector. The analogous valence bond reconnection rules in this new basis must remain simple for the algorithm to work successfully.

To study bipartite spin-half antiferromagnets with N_B B-sublattice sites, $N_A = N_B + 1$ A-sublattice sites, and a doublet ground state in the $S_{total} = 1/2$ sector, we choose the basis

$$\{|\mathcal{A}, a_f\sigma\rangle\} \equiv \{|[\mathcal{A}(b_1)b_1], [\mathcal{A}(b_2)b_2] \ldots [\mathcal{A}(b_{N_B})b_{N_B}]; a_f\sigma\rangle\} \tag{2.6}$$

Each of the basis states in the set above has one A-sublattice spin $\mathbf{S}_{a_f}$ in either the $|a_f\sigma = \uparrow\rangle \equiv |S^z_{a_f} = +1/2\rangle$ or the $|a_f\sigma = \downarrow\rangle \equiv |S^z_{a_f} = -1/2\rangle$ state along the quantisation axis $\hat{z}$, while the N_B spins $\mathbf{S}_{b_i}$ on the B-sublattice sites each form a valence bond singlet state

$$|[\mathcal{A}(b_i)b_i]\rangle \equiv \frac{(|\mathcal{A}(b_i)\uparrow, b_i\downarrow\rangle - |\mathcal{A}(b_i)\downarrow, b_i\uparrow\rangle)}{\sqrt{2}} \tag{2.7}$$

with a partner $\mathbf{S}_{\mathcal{A}(b_i)}$ on the A-sublattice. All basis states are obtained by allowing all possible a_f, two choices for σ, and all possible 'matching' functions $\mathcal{A}$ consistent with a given choice of 'free spin' a_f. Note that for spin conserving Hamiltonians there are two disjoint set of states in this basis which do not mix with each other,

$$\{|\mathcal{A}, a_f\uparrow\rangle\} \equiv \{|[\mathcal{A}(b_1)b_1], [\mathcal{A}(b_2)b_2] \ldots [\mathcal{A}(b_{N_B})b_{N_B}]; a_f\uparrow\rangle\} \tag{2.8}$$

and

$$\{|\mathcal{A}, a_f \downarrow\rangle\} \equiv \{|[\mathcal{A}(b_1)b_1], [\mathcal{A}(b_2)b_2] \ldots [\mathcal{A}(b_{N_B})b_{N_B}]; a_f \downarrow\rangle\}. \tag{2.9}$$

These two sets correspond to the two allowed eigenvalues for the conserved quantum number S^z_{total} in the $S_{total} = 1/2$ sector.

Just like the bipartite valence-bond basis that was used in the original singlet sector algorithm [BS06, SE10], this extended basis spans the $S_{total} = 1/2$ sector and is overcomplete. To prove completeness, let us consider adding one extra B-sublattice site b_{N_B+1} to our system to make the total number of spins even. The singlet sector of this larger system is spanned by the overcomplete bipartite valence bond basis with $N_B + 1$ bonds present in each basis state. States in this larger set are in one-to-one correspondence with possible pair-wise matchings $\mathcal{P}$ that 'find' a A-sublattice 'partner' $\mathcal{P}(b_i)$ for each B-sublattice site b_i to form a singlet:

$$|\mathcal{P}\rangle \equiv |[\mathcal{P}(b_1)b_1], [\mathcal{P}(b_2)b_2] \ldots [\mathcal{P}(b_{N_B+1}b_{N_b+1})]\rangle \tag{2.10}$$

Now, by the laws of angular momentum addition, singlet states of the larger system can only arise from tensor products of the additional spin-half variable at site b_{N_b+1} with the $S_{total} = 1/2$ states of the smaller system. Therefore, to show overcompleteness of our proposed basis for the smaller system, we only need to check whether all states in the bipartite valence bond basis of the larger system are obtainable as tensor products of states of the additional spin $\mathbf{S}_{b_{N_b+1}}$ with states in our proposed $S_{total} = 1/2$ basis. This can be shown by identifying a_f with $\mathcal{P}(b_{N_b+1})$ and $\mathcal{A}$ with the restriction of $\mathcal{P}$ to the domain $(b_1, b_2, \ldots b_{N_b})$. Thus, the set of states defined in (2.7) is an overcomplete basis for the $S_{total} = 1/2$ sector and is a possible generalisation of the original bipartite valence bond basis for the singlet sector.

For $SU(2)$ symmetric spin Hamiltonians of the form (2.2), we use half the basis states $\{|[\mathcal{A}(b_1)b_1], [\mathcal{A}(b_2)b_2] \ldots [\mathcal{A}(b_{N_B})b_{N_B}]; a_f \uparrow\rangle\}$ that only span the $S^z_{total} = 1/2$, $S_{total} = 1/2$ sector a system with $N_A = N_B + 1$ spin-1/2s on the A-sublattice, and N_B spin-1/2s on the B sublattice.

2.2.2 Overlaps and operators

Let us now describe the formulae for the wavefunction overlaps between basis states, and for the action of exchange operators when working in

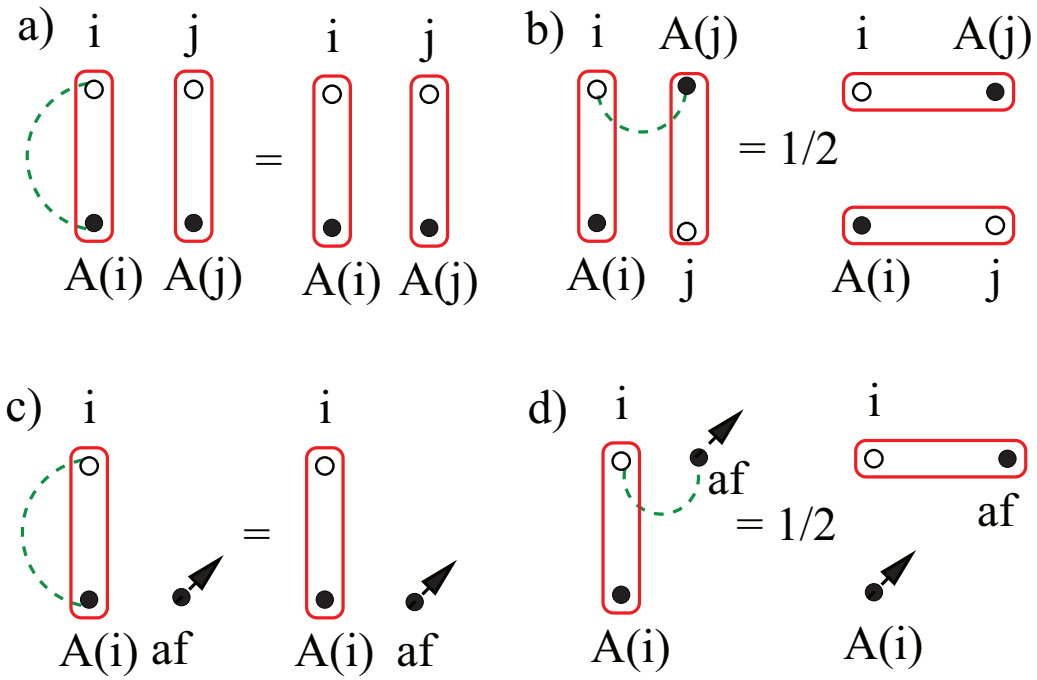

Figure 2.3: Action of singlet Projector P_{ij} (shown as dotted line in the figure) acting on two sites i and j.

the $S_{total} = 1/2$ sector. The wavefunction overlap between two bipartite VB basis states $|\mathcal{P}\rangle$ and $|\mathcal{P}'\rangle$ of the singlet-sector basis are determined by the number of cycles needed to go from the permutation $\mathcal{P}$ to the permutation $\mathcal{P}'$. More pictorially, one may consider the overlap diagram of the two valence-bond covers viewed as 'complete dimer covers' or 'perfect' matchings. This overlap diagram contains N_{loop} (closed) loops of various lengths l_μ, such that each site is part of exactly one loop (see Fig 2.3). Then the amplitude of the corresponding wavefunction overlap, $\langle \mathcal{P}|\mathcal{P}'\rangle = 2^{N_{\text{loop}}}/2^{N_s/2}$, where N_s, the total number of spins is assumed even.

Generalizing this, for the states in our basis for the $S_{total} = 1/2$ sector, we note that the corresponding picture is now in terms of the overlap diagram of two *partial valence bond covers* $(\mathcal{A}, a_f)$ and $(\mathcal{A}', a'_f)$, each of which has one site free, which is not part any valence bond. Such an overlap diagram must have a single 'open string' of length l_f connecting a_f to a'_f, in addition to N_{loop} (closed) loops of various lengths l_α (see Fig 2.3). An elementary calculation reveals that the wavefunction overlap in our $S_{total} = 1/2$ case is given as $\langle \mathcal{A} a_f \sigma | \mathcal{A}' a'_f \sigma' \rangle = \delta_{\sigma\sigma'} 2^{N_{\text{loop}}}/2^{(N_s-1)/2}$, with N_s, the number of sites, now taken to be odd.

The original singlet sector algorithm cleverly utilizes [San05, SE10] the particularly simple action of operators $P_{ij} = \eta_i \eta_j \mathbf{S}_i \cdot \mathbf{S}_j + 1/4$ on basis states $|\mathcal{P}\rangle$. Here $\eta_i = +1$ ($\eta_i = -1$) for i belonging to the A-sublattice (B-sublattice), and thus, the operator $P_{a_\alpha b_\beta}$ that connects an A-sublattice site a_α to a B-sublattice site b_β is precisely the projection operator that projects to the singlet state of the two spins $\mathbf{S}_{a_\alpha}$ and $\mathbf{S}_{b_\beta}$.

The key property of the extended valence bond basis for the $S_{total} = 1/2$ sector, which helps generalise this algorithm to the the $S_{total} = 1/2$ case, is that the action of P_{ij} on the basis states is completely analogous to that in the original valence bond basis for the singlet sector. The new rule are as follows: If neither i nor j correspond to the 'free' spin, P_{ij} acts

in the same manner as in the earlier singlet sector case (Fig 2.3(a,b)):

$$\begin{aligned}
P_{\mathcal{A}(b_\alpha)b_\alpha}|...[\mathcal{A}(b_\alpha)b_\alpha]... ; a_f \uparrow\rangle &= |...[\mathcal{A}(b_\alpha), b_\alpha]... ; a_f \uparrow\rangle, \\
P_{\mathcal{A}(b_\alpha)b_\beta}|...[\mathcal{A}(b_\alpha), b_\alpha]...[\mathcal{A}(b_\beta), b_\beta]... ; a_f \uparrow\rangle &= \frac{1}{2}|...[\mathcal{A}(b_\alpha), b_\beta]...[\mathcal{A}(b_\beta), b_\alpha]... ; a_f \uparrow\rangle, \\
P_{\mathcal{A}(b_\alpha)\mathcal{A}(b_\beta)}|...[\mathcal{A}(b_\alpha), b_\alpha]...[\mathcal{A}(b_\beta), b_\beta]... ; a_f \uparrow\rangle &= \frac{1}{2}|...[\mathcal{A}(b_\alpha), b_\beta]...[\mathcal{A}(b_\beta), b_\alpha]... ; a_f \uparrow\rangle, \\
P_{b_\alpha b_\beta}|...[\mathcal{A}(b_\alpha), b_\alpha]...[\mathcal{A}(b_\beta), b_\beta]... ; a_f \uparrow\rangle &= \frac{1}{2}|...[\mathcal{A}(b_\alpha), b_\beta]...[\mathcal{A}(b_\beta), b_\alpha]... ; a_f \uparrow\rangle.
\end{aligned} \tag{2.11}$$

On the other hand, if either i or j correspond to the free site a_f, the projection rules are as follows (Fig 2.3(c,d)):

$$\begin{aligned}
P_{a_f b_\alpha}|...[\mathcal{A}(b_\alpha)b_\alpha]... ; a_f \uparrow\rangle &= \frac{1}{2}|...[a_f, b_\alpha]... ; \mathcal{A}(b_\alpha) \uparrow\rangle, \\
P_{a_f \mathcal{A}(b_\alpha)})|...[\mathcal{A}(b_\alpha)b_\alpha]... ; a_f \uparrow\rangle &= \frac{1}{2}|...[a_f, b_\alpha]... ; \mathcal{A}(b_\alpha) \uparrow\rangle.
\end{aligned} \tag{2.12}$$

Thus, when none of the sites i, j contains the free spins, P_{ij} acts in exactly the same way as in the earlier singlet sector basis. In case one these two sites i, j has the free spin, P_{ij} reconnects with amplitude $1/2$. The important thing to note is that these rules are completely analogous to the original singlet sector case, so that the Monte Carlo technique remains essentially the same, except for the fact that a loop configuration now includes an open string connecting the free sites on the left and right trial states. This string has only one orientation as compared to the two possible orientations of the closed loops.

By analogy to the original singlet sector work [BS06], this allows us to use the following prescription for the calculation of $\langle \mathcal{A}' a'_f \uparrow | P_{ij} | \mathcal{A} a_f \uparrow \rangle$ between two of our basis states: We write $\langle \mathcal{A}' a'_f \uparrow | P_{ij} | \mathcal{A} a_f \uparrow \rangle = W_{ij} \langle \mathcal{A}' a'_f \uparrow | \mathcal{A} a_f \uparrow \rangle$ and develop rules for the weight W_{ij}. W_{ij} is fixed by comparing the overlap diagram of $(\mathcal{A}' a'_f \uparrow)$ and $(P_{ij} | \mathcal{A} a_f \uparrow)$ with the original overlap diagram of $(\mathcal{A}' a'_f \uparrow)$ and $(\mathcal{A} a_f \uparrow)$. If the action of P_{ij} makes no changes in the original overlap diagram, $W_{ij} = 1$. Also, if a loop is split into two loops or the open string is split into one loop and another open string, $W_{ij} = 2 \times 1/2 = 1$ (here, the factor of two comes from the fact that the number of loops in the overlap diagram increases by one, while the factor of half is the reconnection amplitude from Eqn 2.12). On the other

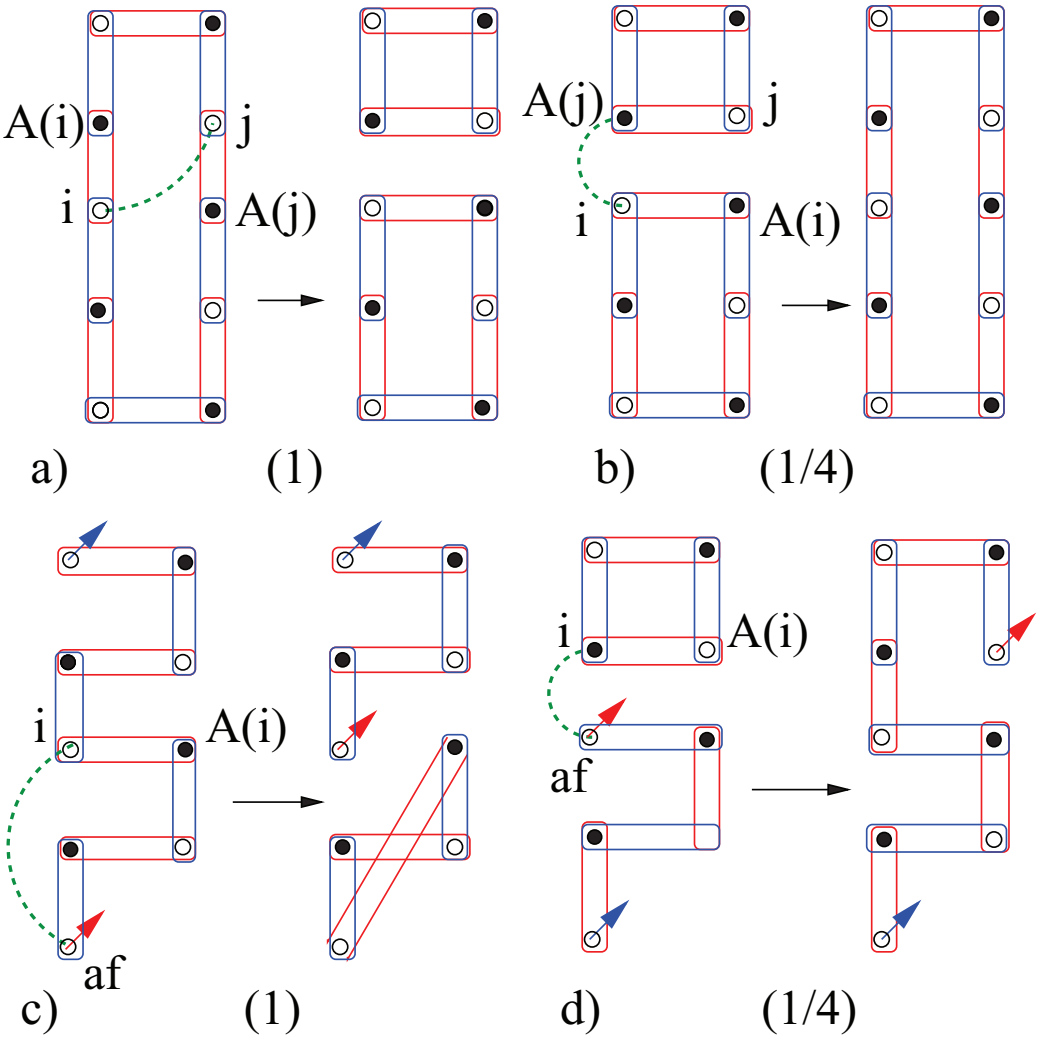

Figure 2.4: Action of a singlet projector on the overlap loops for closed loops (a, b) and open string (c,d). Corresponding weights are given within parenthesis.

hand, if two loops merges into one, or if the open string fuses with a loop to give a larger open string, then $W_{ij} = (1/2) \times (1/2)$, where the first factor of half is due the reduction of the number of loops by one, and the second factor of one-half comes due the reconnection taking place2.12. These rules are tabulated in Fig 2.4, and the important thing to note is that the open string can be treated on equal footing with closed loops in all cases, allowing one to generalise the singlet sector rules directly to the $S_{total} = 1/2$ sector case discussed here.

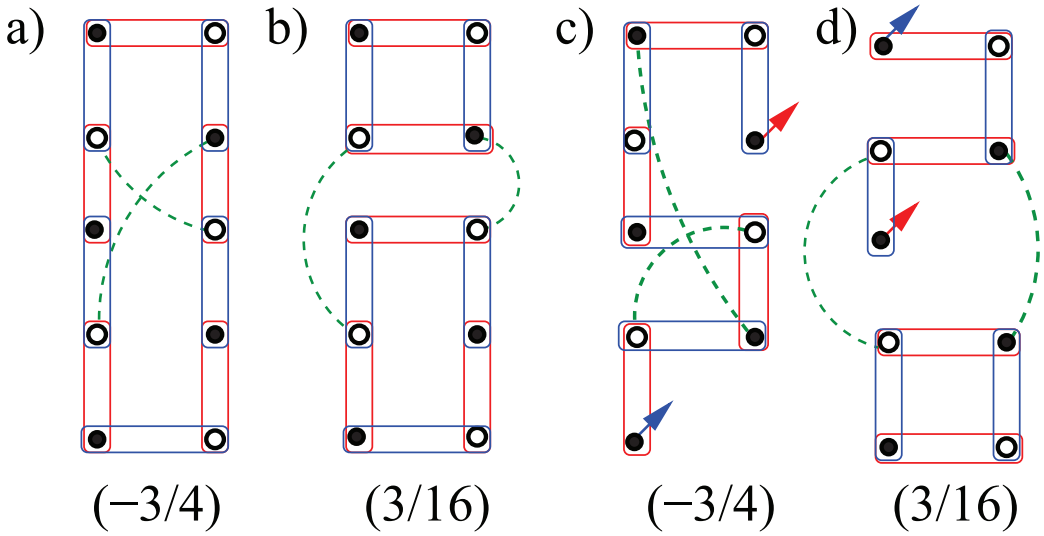

Figure 2.5: Overlap graphs contributing to the estimator of $\langle(\vec{m}_s^2)^2\rangle \equiv \sum_{ijkl}(P_{ij} - 1/4)(P_{kl} - 1/4)\rangle$ with corresponding values of $W_{ijkl} - W_{ij}W_{kl}$ (defined in text) given within parenthesis.

2.2.3 Estimators

As in the singlet sector case [San05, BS06, SE10], physical properties can be calculated by taking each Monte Carlo configuration of loop diagrams generated by the algorithm and generating the overlap diagram at the center that represents the overlap of $\prod_{\tau=1}^{m} H_{b_\tau}^{\sigma_\tau}|\psi_{1/2\uparrow}\rangle$ with $\langle\psi_{1/2\uparrow}\prod_{\tau=m+1}^{2m} H_{b_\tau}^{\sigma_\tau}$. Only difference being the presence of a single string along with the loops.

Consider for instance the Neel order parameter $\vec{m}_s = \sum_i \eta_i \vec{S}_i$. Clearly, $\langle m_s^x\rangle = \langle m_s^y\rangle = 0$. However, $\langle m_s^z\rangle$ receives contributions from sites on the open string in the overlap diagram, since the open string, in contrast to (closed) loops, has only one orientation. More formally, we may write $\langle \mathcal{A}'a'_f \uparrow |S_i^z|\mathcal{A}a_f \uparrow\rangle = W_i\langle \mathcal{A}'a'_f \uparrow |\mathcal{A}a_f \uparrow\rangle$ and note that $W_i = \eta_i/2$ if i is part of the open string in the overlap diagram between $(\mathcal{A}'a'_f)$ and $(\mathcal{A}a_f)$ and 0 otherwise. We thus have,

$$\langle m_s^z\rangle \;=\; \frac{\langle l_f\rangle}{2} \tag{2.13}$$

where the angular brackets on the right denote the ensemble average over the ensemble of overlap diagrams generated by the modified $S_{total} = 1/2$, $S_{total}^z = 1/2$ sector Monte Carlo algorithm outlined above.

We now turn to $\langle \vec{m}_s^2 \rangle = \langle \sum_{ij} (P_{ij} - 1/4) \rangle$. As noted earlier, whenever i and j are both in the open string or the same (closed) loop, the corresponding weight $W_{ij} = 1$, while $W_{ij} = 1/4$ when i and j do not both belong to the open string or the same (closed) loop. For an overlap diagram with closed loops of lengths l_α (with $\alpha = 1, 2 \ldots N_l - 1$) and an open string of length $l_{N_l} \equiv l_f$, the latter can occur in $\sum'^{N_l}_{\alpha,\beta=1} l_\alpha l_\beta$ ways where the prime on the sum indicates that $\alpha = \beta$ is disallowed, while the former can occur in $\sum_{\alpha=1}^{N_l} l_\alpha^2$ ways. As in the singlet sector case, we thus obtain $\langle \vec{m}_s^2 \rangle = \langle \frac{1}{4} \sum'^{N_l}_{\alpha,\beta=1} l_\alpha l_\beta + \sum_{\alpha=1}^{N_l} l_\alpha^2 - \frac{1}{4} \sum_{\alpha,\beta=1}^{N_l} l_\alpha l_\beta \rangle$, where the angular brackets on the right indicate average over the ensemble of overlap diagrams generated by the algorithm. This reduces to

$$\langle \vec{m}_s^2 \rangle = \langle \frac{3}{4} \sum_{\alpha=1}^{N_l} l_\alpha^2 \rangle \tag{2.14}$$

where the angular brackets on the right again denote averaging over the ensemble of overlap diagrams generated by the algorithm, and the important thing to note is that this estimator looks the same as the one in (2.4) and that the open string ($\alpha = N_l$) is treated on the same footing as the closed loops ($\alpha = 1, 2, \ldots N_l - 1$).

Proceeding as above, we construct the estimator for the ground state expectation value of the fourth power of the Neel order parameter, *i.e* $\langle (\vec{m}_s^2)^2 \rangle$. To derive this estimator in the $S_{total} = 1/2$ sector, we follow Sandvik and Beach [BS06], and write $\langle (\vec{m}_s^2)^2 \rangle = \langle \sum_{ij} \sum_{kl} (P_{ij} - 1/4)(P_{kl} - 1/4) \rangle$. As in Ref [BS06], we note that the estimator for this quantity differs from the square of the estimator for $\vec{m}_s^2$ only when the actual weight $W_{ijkl} \equiv \langle \mathcal{A}' a'_f \uparrow | P_{ij} P_{kl} | \mathcal{A} a_f \uparrow \rangle / \langle \mathcal{A}' a'_f \uparrow | \mathcal{A} a_f \uparrow \rangle$ differs from the product $W_{ij} W_{kl}$ of the independent weights $W_{ij} \equiv \langle \mathcal{A}' a'_f \uparrow | P_{ij} | \mathcal{A} a_f \uparrow \rangle / \langle / \mathcal{A}' a'_f \uparrow | \mathcal{A} a_f \uparrow \rangle$ and W_{kl} (defined analogously to W_{ij}). As in the singlet sector case, this happens only in the two cases shown in Fig 2.5, where the difference $W_{ijkl} - W_{ij} W_{kl}$ has been tabulated. Thus, the only new calculation needed is a count of the number of ways in which each of the cases Fig 2.5 (a), (b), (c), (d) arise, weighted by the corresponding values of $W_{ijkl} - W_{ij} W_{kl}$. It is at this step that the open string needs to be treated separately as this this counting for a open string in Fig 2.5 (c) gives different result from the analogous counting for a closed loop in Fig 2.5 (a) by precisely one: Fig 2.5 (a) can arise in $\frac{1}{3} l_\alpha^4 - \frac{4}{3} l_\alpha^2$ ways, while Fig 2.5 (c) can arise in $\frac{1}{3} l_f^4 - \frac{4}{3} l_f^2 + 1$ ways. On the other hand, both Fig 2.5 (b) and (d) arise in

precisely $2l_\alpha^2 l_\beta^2$ ways (with $l_\beta \equiv l_f$) for Fig 2.5 (d).

With all this in hand, we obtain

$$\begin{aligned}\langle(\vec{m}_s^2)^2\rangle &= \langle(\frac{3}{4}\sum_{\alpha=1}^{N_l} l_\alpha^2)^2\rangle + \\ &\frac{6}{16}\sum_{\alpha,\beta=1}^{N_l}{}' \langle l_\alpha^2 l_\beta^2\rangle - \frac{1}{4}\sum_{\alpha=1}^{N_l}\langle l_\alpha^4 - 4l_\alpha^2\rangle - \frac{3}{4}\,,\end{aligned} \tag{2.15}$$

which reduces to,

$$\langle(\vec{m}_s^2)^2\rangle = \sum_{\alpha=1}^{N_l}\langle -\frac{5}{8}l_\alpha^4 + l_\alpha^2\rangle + \frac{15}{16}\langle(\sum_{\alpha=1}^{N_l} l_\alpha^2)^2\rangle - \frac{3}{4}. \tag{2.16}$$

Again, remarkably, the presence of the open string only changes the estimator by the addition of a constant $(-\frac{3}{4})$ when compared to the corresponding expression in the singlet sector case [BS06].

2.3 Benchmarks, Illustrative Results and Outlook

We test the extended projector valence bond Monte Carlo for the $S_{total} = 1/2$ sector method described above by comparing estimated observables with exact numerical results for small systems. We have implemented this Monte Carlo technique with efficient loop updates [SE10] for square lattice Heisenberg antiferromagnet on a $L_x \times L_y$ with both L_x, L_y odd and boundaries open. We have also simulated, using this new technique, a $L \times L$ square lattice Heisenberg antiferromagnet with periodic boundary conditions and L even, but with one site missing. We compare the results for i) a $L_x = 3$, $L_y = 5$ open boundary condition system, ii) and a $L = 4$ period boundary condition system having one site missing, with results obtained in exact diagonalisation. In Fig 2.6, we show the dependence of the estimators for ground state energy, and $S_z(\pi, \pi)$ as a function of the projection power m in both these cases. It is clearly seen that the Monte Carlo estimates do converge to the exact values for both the observables and in both of the models.

We investigate the efficiency of the modified algorithm, as far as the convergence of various physical observables to their ground state values

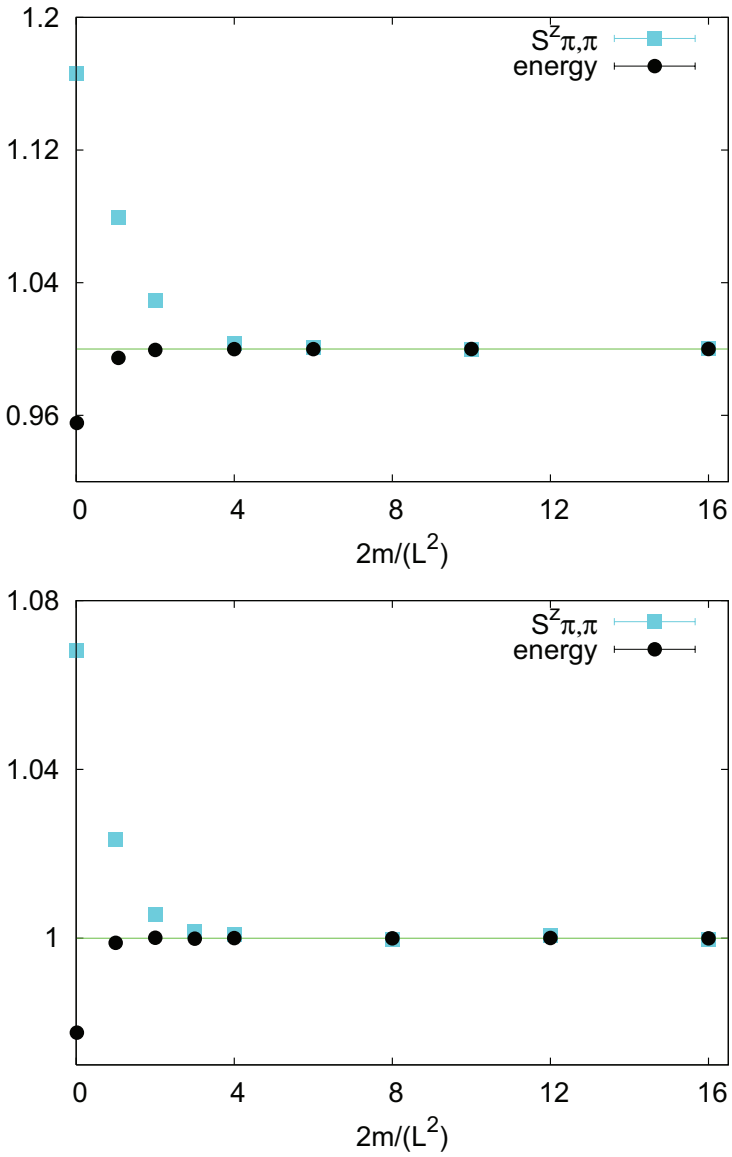

Figure 2.6: Variation of the Monte Carlo estimates of $S_z(\pi,\pi)$ and energy of the $2d$ $S = 1/2$ Heisenberg antiferromagnet (normalized by their respective exact values obtained from exact diagonalization) plotted as a function of projection length $2m$ normalized by the system volume $L^2 \equiv L_x \times L_y$: for a 3×5 open system (top panel) and a 4×4 periodic system with one site removed(bottom panel).

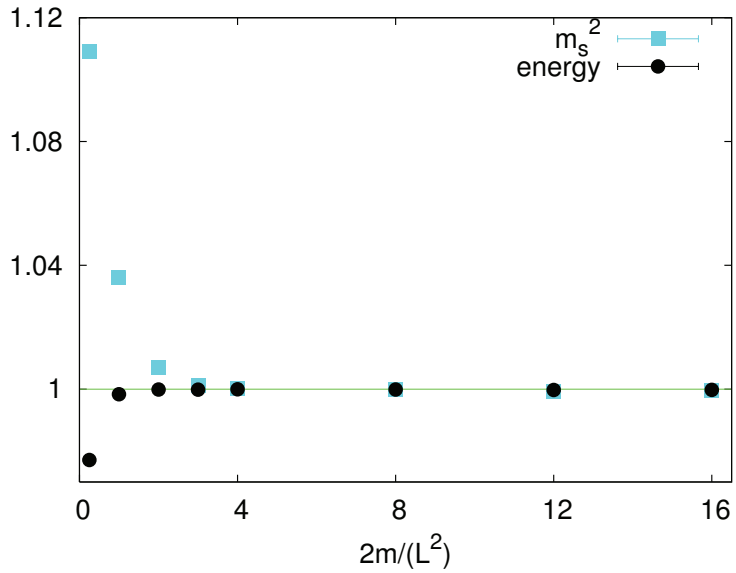

Figure 2.7: Variation of the Monte Carlo estimates of the energy and $\langle \vec{m}_s^2 \rangle$, the ground state expectation value of the square of the antiferromagnetic order parameter, of the $2d$ $S = 1/2$ Heisenberg antiferromagnet, normalized by their exact values obtained from exact diagonalisation, plotted as a function of projection length $2m$ normalized by system volume $L^2 = L_x L_y$, for a 4×4 periodic system.

is concerned, by comparing with the performance of the original singlet sector method for similar system sizes. We show in Fig 2.7 a study of the performance of the original singlet sector algorithm for a $L = 4$ periodic boundary condition system. From these comparisons, it is clear that the performance of the modified algorithm is comparable to the performance of the original algorithm in the singlet sector, and thus our modification provides a useful method to study a $S_{total} = 1/2$ ground state of finite size antiferromagnets.

3

$S = 1/2$ Heisenberg antiferromagnet with open boundaries

In spite of a large body of existing work on the $S = 1/2$ square lattice Heisenberg model, this particular model has been the focus of many recent studies, in the context of experiments on antiferromagnets doped with non-magnetic impurities [ABGH09, HKP+99, KBB+92, CRT+95, VMG+02]. In these experiments, a transition from long range ordered state to a disordered state is observed as doping concentrations cross the percolation threshold [VMG+02]. Although, near the impurity sites, a model with only near neighbour Heisenberg exchange interactions between the spin moments does not fully capture the microscopic details, the site diluted near neighbour Heisenberg model turns out to be a reasonably good first approximation to describe these systems. This has motivated a recent revival of study of finite size square lattice $S = 1/2$ Heisenberg model with finite boundaries [KTH+00, San02, WS10, ZGW+10]. In this context, the singlet sector valence bond projector Monte Carlo and its spin-half counterpart could be very useful.These simulation techniques are also suitable to study clusters with arbitrary shapes. With this motivation, in this chapter, we concentrate on the finite size effects in $S = 1/2$ square lattice Heisenberg model and antiferromagnet in general. For simplicity, we study odd by odd systems with open boundary condition and use the Monte Carlo technique described in the last chapter to study their magnetic properties. The subsequent presentation is based on joint work with Sambuddha Sanyal and Kedar Damle (manuscript under preparation).

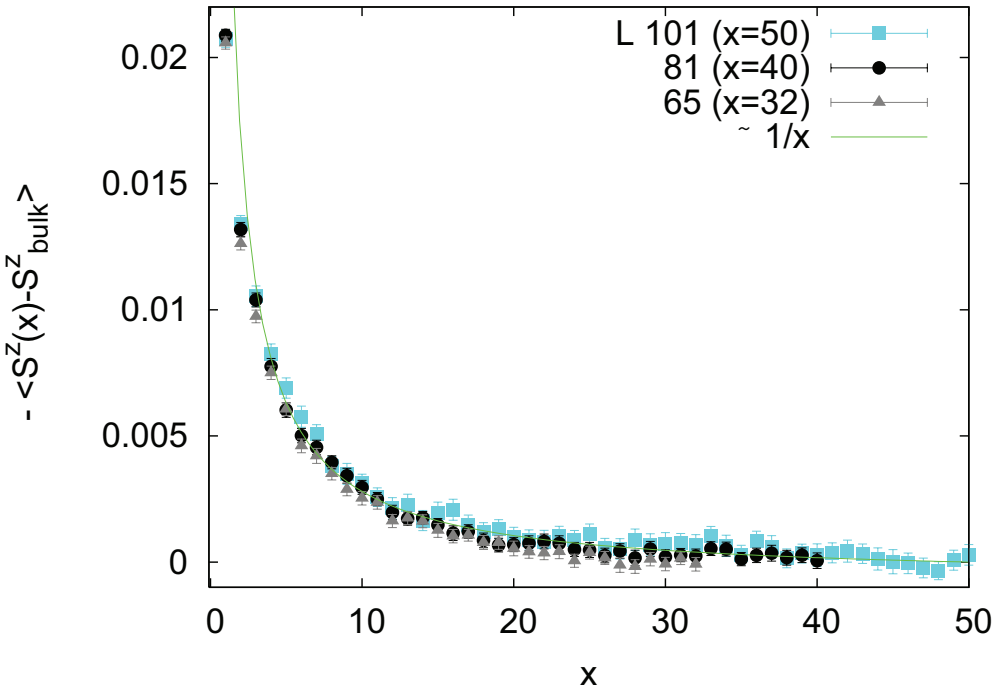

Figure 3.1: Boundary induced depletion of the alternating spin texture decays as inverse power of the perpendicular distance from the boundary for pure Heisenberg model on a square lattice with open boundaries.

3.1 Simulations and measurements

We have implemented the total spin half sector valence bond Monte Carlo [BD10] for square lattice Heisenberg model and also several other model antiferromagnets where some competing interactions reduce the magnetic order, but still support long range AF order, e.g. JJ' model and JQ models (defined later). Our system sizes range from 11×11 to 101×101, and projection length scales as cubic power of linear system size to ensure convergence to the ground state. We perform $\gtrsim 10^5$ equilibration steps followed by $\gtrsim 10^6$ Monte Carlo measurements.

To study the magnetic properties of these finite size systems in the $S_{total} = 1/2$ sector, we focus on the local spin texture, $S_z(x,y)$, and its Fourier transform at antiferromagnetic wave vector (π,π), $S_z(\pi,\pi) = \left(\sum_{x,y}(-1)^{(x+y)}S_z(x,y)\right)$. We have also studied the antiferromagnetic order parameter $\mathbf{m}_s^2 = \left(\sum_{x,y}(-1)^{(x+y)}\mathbf{S}(\mathbf{r})\cdot\mathbf{S}(\mathbf{r}+(x,y))\right)$ for periodic sys-

tems.

3.2 Results

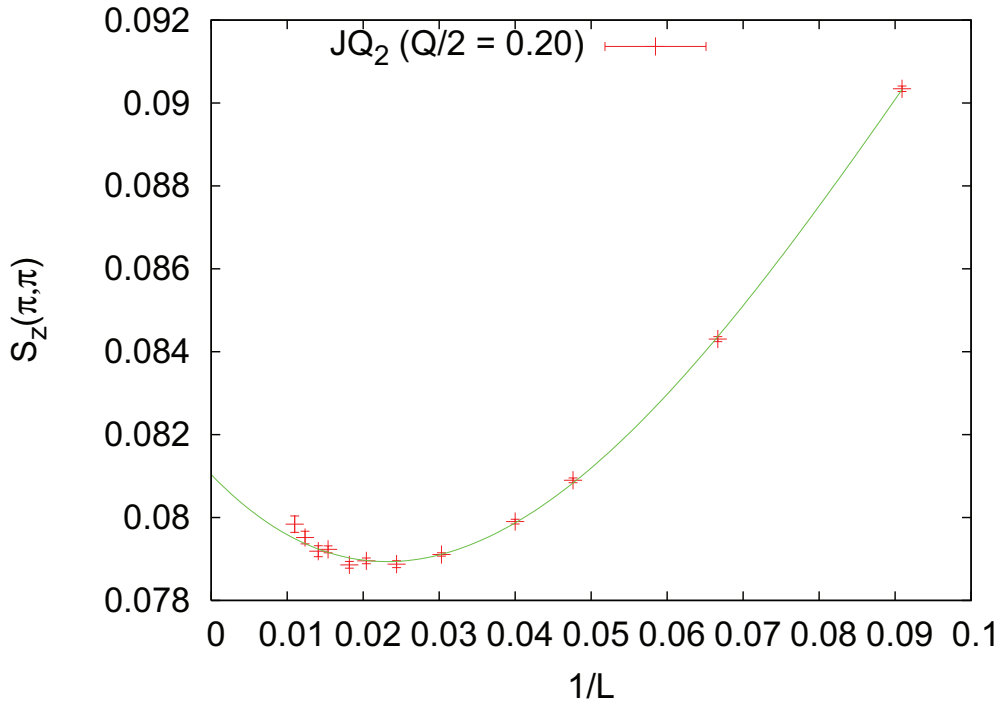

Figure 3.2: An illustrative example of nonmonotonic finite size corrections of $S_z(\pi, \pi)$, observed in the antiferromagnetic phase. The data shown here is for JQ_2 model and value Q is chosen so that the system is deep in the antiferromagnetic phase. The cubic polynomial fitting curve is also shown as a solid line.

3.2.1 Edge effects

Metlitski and Sachdev[MS08] have studied quantum antiferromagnets in a semi-infinite geometry using nonlinear sigma model effective description of quantum antiferromagnets. They predict that the antiferromagnetic order is suppressed near the boundary and this suppression decays as inverse power of the perpendicular distance from the boundary. They

also verify their predictions using the spin wave approximation technique. Our measurements of spin textures in antiferromagnets with open boundaries confirm their prediction. This $\sim 1/r$ decay of the alternating spin texture is shown in Fig. 3.1. Although, It must be noted that our measurements are performed in the $S_{total} = 1/2$ sector, and the texture is not really the local antiferromagnetic order parameter. But, as we shall see below, the alternating part of the texture ($S_z(\pi, \pi)$) is intimately related to the staggered magnetisation m_s, and in fact, can be used as a thermodynamic order parameter.

3.2.2 Magnetisation order parameter

Data for $S_z(\pi, \pi)$, obtained by simulating finite size samples of odd by odd square lattice $S = 1/2$ Heisenberg model, shows that in the $L \to \infty$ limit, $S_z(\pi, \pi)$ extrapolates to a finite value. But the approach to the thermodynamic limit has an intriguing non-monotonic behaviour. To obtain the accurate thermodynamic value of this observable, it is necessary to fit the finite size data to a third order polynomial in $1/L$. We find that same feature in the finite size $S_z(\pi, \pi)$ data for the other models studied here, as long as the additional interactions are weak enough so that the system still remains antiferromagnetic. In Fig. 3.2 we show examples of this peculiar behaviour of the finite size corrections in $S_z(\pi, \pi)$. The finite size values, $S_z(\pi, \pi, L)$ approach the thermodynamic value in a nonmonotonic way, so that at least a third order ploynomial in $1/L$ is needed to fit the finite size data.

It is well known that quantum antiferromagnets are universally described by an effective non linear sigma model[Sac01] field theory. Also, as we have seen, the expectation values of $S_z(\pi, \pi)$ for open lattice antiferromagnet has a finite thermodynamic limit. Both these facts put together, lead us to conjecture a universal relationship between thermodynamic limit values of $S_z(\pi, \pi)$ for open systems and that of staggered magnetisation m_s for periodic systems. This relationship is expected to hold independent of the model Hamiltonian as long as the system is deep enough in the antiferromagnetic phase. Fig. 3.3 shows plots of $S_z(\pi, \pi)$ versus m_s for three different models, which verify this claim to within numerical accuracy. Here the $S_z(\pi, \pi)$ data is obtained by simulating the models on an odd by odd square lattice and extrapolating the finite size values to the thermodynamic limit. The corresponding m_s data are obtained from simulations of periodic systems at the same values of the coupling

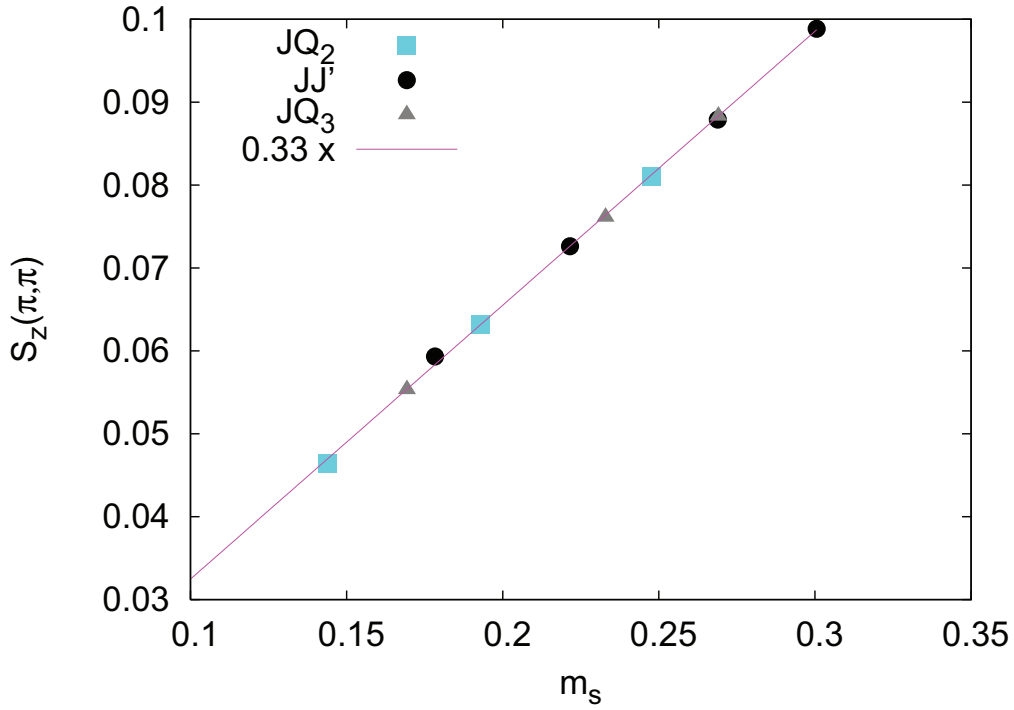

Figure 3.3: Extrapolated thermodynamic values of $S_z(\pi,\pi)$ for various models of antiferromagnets on an open lattice, plotted as function of staggered magnetisation m_s for the same models on periodic lattices. The former is clearly an universal function of the later, and deep in the antiferromagnetic phase, this universal function can be well approximated by a straight line.

constants.

3.3 Summary

Using the extended valence bond quantum Monte Carlo method, we study the ground state staggered magnetisation of the $S = 1/2$ near-neighbour Heisenberg model on $L \times L$ square lattices with L odd. We measure the spatial spin texture $\langle S_z(x,y)\rangle$, in the $S_{total} = 1/2$ ground state. We find that the boundary induced deviation of spin-texture from bulk value decays as inverse power of perpendicular distance from the boundary. This is in agreement with earlier theoretical predictions[MS08].

We also study square lattice JQ models and JJ' model deep in the

antiferromagnetic phase. Our result reveal interesting nonmonotonic behaviour of the finite size corrections in $S_z(\pi, \pi)$. In the antiferromagnetic phase $S_z(\pi, \pi)$ extrapolates to a finite value and this extrapolated thermodynamic value of $\langle S_z(\pi, \pi) \rangle$ is solely determined by the value of antiferromagnetic order parameter m_s for periodic systems - the former being an universal linear function of the latter.

4

Deconfined Quantum Critical Transition

Within the Landau-Ginzburg-Wilson paradigm, phase transitions are described by a phenomenological Landau free-energy functional [CL98]. This free energy is a polynomial in the order parameter field/fields, and obtained by demanding consistency with all the symmetries of the problem. In case of a transition from one ordered phase to another, such that the respective order parameters break different symmetries, Landau theory predicts a generic first order transition or a region of phase coexistence. This Landau theory expectation is violated in the proposed scenario of deconfined critical points[SVB+04, SBS+04], where there is a direct continuous transition from a spin symmetry broken antiferromagnetic phase to a translational symmetry broken valence bond solid phase. Numerical evidence for a continuous transition in the proposed field theory describing this transition is controversial [MV08] and a counter-claim of a weakly first order transition exists [KMP+08] in the literature. But the JQ models proposed by Sandvik seem to provide a microscopic model where such a continuous transition takes place [San07, MK08, LSK09]. Refuting earlier counter-claims[JNCW08] of a weakly first order transition in this model, Sandvik has recently presented strong evidence in favour of critical scaling with logarithmic corrections at this transition point[San10].

4.1 Landau-Ginzburg theory of continuous phase transitions

Landau-Ginzburg theory is an extremely successful framework to describe phase transitions. The starting point of Landau-Ginzburg phe-

nomenology is to identify the order parameter associated with the phase transition under consideration. The order parameter distinguishes the two phases by having a non-zero expectation value in one of them, and vanishing in the other. It is assumed that this order parameter mode is the most important one near the transition and a phenomenological Landau free energy is constructed as a polynomial of the order parameter with all possible terms consistent with the symmetries of the problem being present. The evolution of the Landau free energy minima as a function of some tuning parameter describes the transition from one phase to another.

For example, let us consider some phase transition characterised by a Z_2 symmetric order parameter m, then the Landau free energy $f(m)$ could be written down as a polynomial in m,

$$f(m) = r\, m^2 + u\, m^4 + \dots \,. \tag{4.1}$$

Note the absence of linear and cubic terms in this polynomial as they are forbidden by the Z_2 invariance of the problem. With $r = r(Q) \sim (Q - Q_c)$, the minima of this free energy describes a continuous transition form a phase above the critical coupling Q_c with $\langle m \rangle = 0$ to a phase below Q_c with $\langle m \rangle \sim \sqrt{r/u}$ (see Fig.4.1). Below Q_c, system undergoes a spontaneous symmetry breaking in the thermodynamic limit and chooses one of the two minima at $\sim \pm\sqrt{r/u}$.

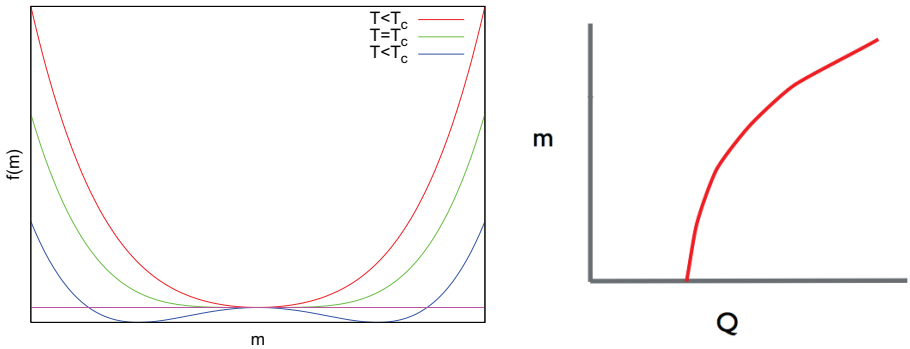

Figure 4.1: Evolution of the minima of Landau free energy $f(m)$ as Q is varied. For $Q \geq Q_c$ the minimum is at $m = 0$, while for $Q \leq Q_c$ a pair of minima appears at $m \sim \pm\sqrt{r/u}$.

4.2 Landau-Ginzburg description of direct transitions between two different symmetry broken phases

The above Landau theory description of phase transitions can easily be generalised to more complex situations with more than on order parameters [CL98]. Let us consider a system with two Z_2 order parameter m_1 and m_2. The most general form of the Landau free energy describing the system is as follows,

$$f(m_1, m_2) = r_1\, m_1^2 + r_2\, m_2^2 + u_1\, m_1^4 + u_2\, m_2^4 + u_{12}\, m_1^2\, m_2^2 + \dots \,. \quad (4.2)$$

To understand nature of phase transitions in this system, let us first consider the limiting case of $u_{12}/(u_1 u_2) \gg 1$. In this limit the two order parameters are essentially noninteracting and expectation values of of m_1 and m_2 become finite as r_1 and $_2$ goes negative respectively as some coupling Q is tuned.

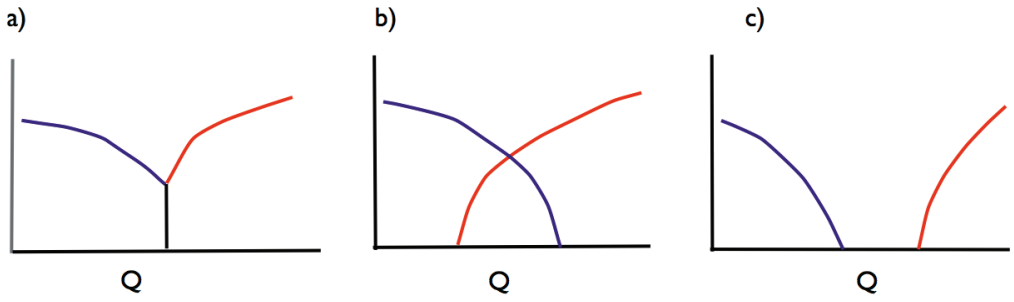

Figure 4.2:

(see Fig. 4.2). In this situation, transition from a phase with $m_1 \neq 0, m_2 = 0$ to another with $m_1 = 0, m_2 \neq 0$ must take place through a phase where both the order parameters are zero or both of them vanish (see Fig. 4.2). Only if the system is tuned to a multicritical point ($r_1 = 0, r_2 = 0$) a simultaneous continuous transition is allowed.

In the opposite limit of $u_{12}/(u_1 u_2) \ll 1$, the region $m_1 \neq 0, m_2 \neq 0$ is not favoured. Then, the transition from a phase with $m_1 \neq 0, m_2 = 0$ to phase with $m_1 = 0, m_2 \neq 0$, is either via a simultaneous first order jump in both the order parameters or through a region where both the order parameters vanish as shown in Fig. 4.2. Just as in the previous case, a direct continuous requires fine tuning to a multicritical point.

Thus, according to the Landau theory, a direct transition between two different symmetry broken phases cannot be continuous, unless the system is tuned to a multicritical point.

4.3 Continuous transitions from Néel ordered phase to valence bond solid phase: Deconfined quantum critical transitions

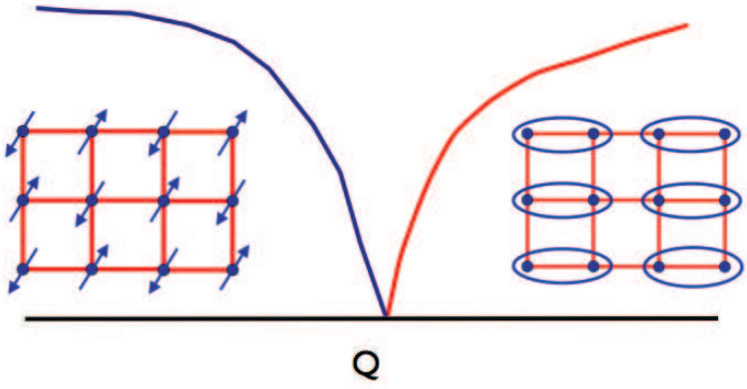

Figure 4.3:

Recently Senthil and co-workers [SVB$^+$04, SBS$^+$04] , partly motivated by numerical work of Sandvik and co-workers [SDSS02, SM06], have proposed a novel continuous phase transitions between a spin-rotation symmetry broken Néel ordered state, and a lattice translation symmetry broken columnar valence-bond solid phase in a bipartite $S = 1/2$ spin system (Fig. 4.3). This violates the simple Landau theory considerations of previous section, which would predict either a first order transition or a region of phase co-existence. Below, we will follow the discussion in Senthil and Levin [LS04], which presents an intuitive picture of this transition in terms of the vortex-like defects in the solid phase.

In the valence bond solid phase, the ground state is four fold degenerate - corresponding to the phase of valence bond solid order parameter being $0, \pi/2, \pi$, or $3\pi/2$ (See Fig. 4.4). In this solid, one can have defects in the form of domain walls, such that the phase changes by $\pi/2$

across the domain walls. If four of these domain walls meet at a point, such that the phase of the complex order parameter winds by 2π around this point of intersection, then that gives us a Z_4 vortex. It turns out that

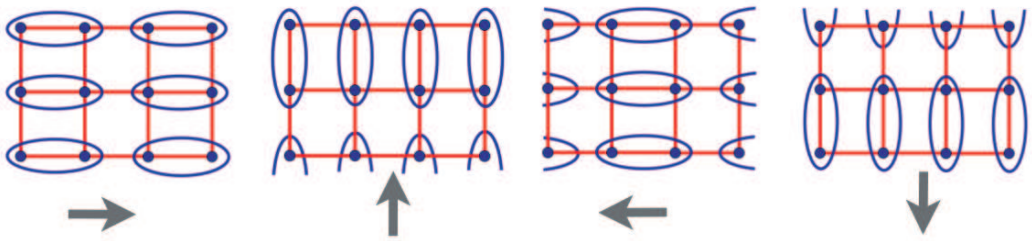

Figure 4.4:

such a vortex must have a free spin-half moment at its core as shown in Fig. 4.5, which can be identified with spinon like $S = 1/2$ excitations. Also, note that upon translation by a lattice spacing a vortex transforms into an antivortex. In the valence-bond solid phase, to separate a vortex-antivortex pair by a finite distance, one must pay a finite energy cost associated with the domain walls, so that the spinons are confined. In fact each valence bond can be thought of as a tightly bound pair of a vortex and an anti-vortex. Deep in the solid phase, it costs finite energy to separate them as it involves creation of domain-walls. As the transition away from solid ordered phase is approached by tuning some coupling constant, domain walls become cheaper and these Z_4 vortex-antivortrex pair unbinds destroying the solid order. Since each of these vortices carry a free spin half moment at their cores, the proliferation of vortices also leads to spin-symmetry breaking: forcing a continuous transition from a lattice-translation symmetry broken phase to a spin-rotation symmetry broken phase.

4.4 Microscopic realisation of Néel-VBS continuous transition:

Following above proposal of a unconventional Néel-VBS transition, Sandvik came up with a model spin Hamiltonian, the JQ model [San07],

$$H_{JQ_2} = -J \sum_{\langle ij \rangle} P_{ij} - Q_2 \sum_{\langle ij,kl \rangle} P_{ij} P_{kl}, \tag{4.3}$$

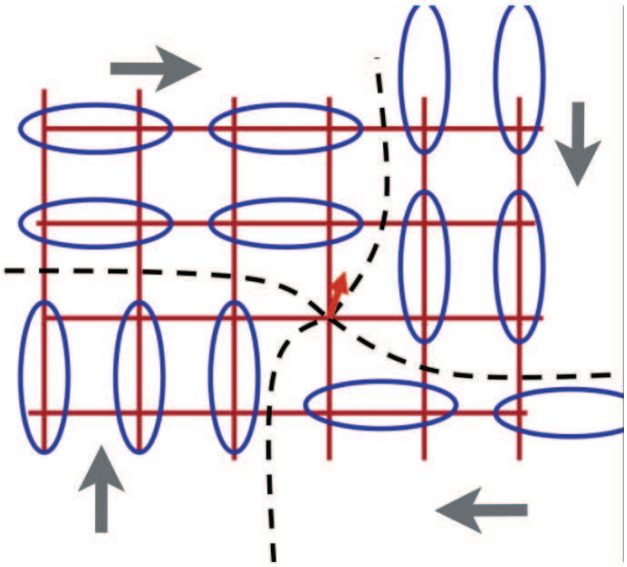

Figure 4.5:

where $P_{ij} = \frac{1}{4} - \mathbf{S}_i \cdot \mathbf{S}_j$ is singlet projector and the sums are over bonds and plaquettes as shown in Fig. 4.6. This is a model where there is a transition between a Néel ordered phase and a valence-bond solid phase. Here, in addition to near-neighbour Heisenberg interactions(J) there is a competing four spin plaquette interaction(Q_2), which favours columnar valence bond solid order as has been shown numerically.

Using valence bond projector Monte Carlo for systems consisting of upto 32×32 spins, Sandvik concluded in favour of a continuous transition from a Néel ordered state to a valence-bond solid state in the JQ_2 model. This claim found support in subsequent finite temperature quantum Monte Carlo studies by Melko and Kaul [MK08], who could access much larger system sizes.

But, in a study of the same model using another finite temperature Monte Carlo method, Jiang et. al. [JNCW08] presented evidence in favour of a weakly first order transition. For example, they showed data that suggested that at the critical coupling, the spin-stiffness ρ_s saturates to a constant value as is expected for a coexistence of the competing orders at a first order transition. At a genuine critical point with dynamic exponent $Z = 1$, ρ_s should vanish as inverse power of system size (L).

But subsequent work by Sandvik et. al. [LSK09] showed that a similar

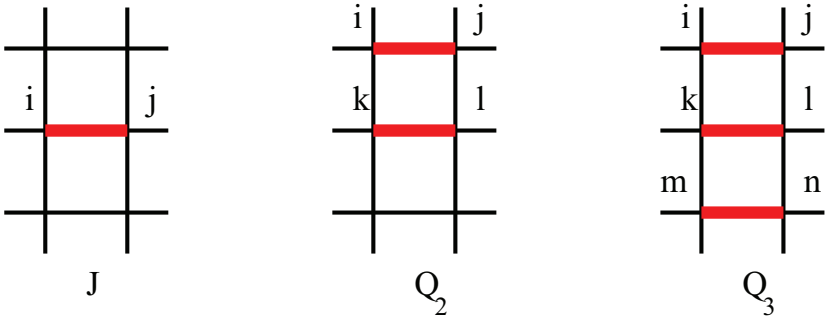

Figure 4.6: Representative bond and plaquette operators in JQ model Hamiltonians. A thick bond denotes a projector acting on that bond. Note that all symmetry related bond and plaquette operators are also present in the Hamiltonian.

transition is seen in the related JQ_3 model, where the plaquette interactions involve six spins of three neighbouring parallel bonds(see Fig. 4.6),

$$H_{JQ_3} = -J \sum_{\langle ij \rangle} P_{ij} - Q_3 \sum_{\langle ij,kl,nm \rangle} P_{ij} P_{kl} P_{nm}. \tag{4.4}$$

The scaling exponents obtained in this transition, matched within statistical errors to those of the JQ_2 transition, providing evidence in favour of a universal deconfined quantum critical description of the Néel-VBS transition in JQ models. But the doubt raised by Jiang et. al. [JNCW08] remained unanswered. In addition simulations of various lattice regularisations of the field theory proposed by Senthil et. al. to describe the transition did not agree on the nature of the transition. Kuklov and coworkers claimed it to be a weak first order transition [KMP$^+$08], while Motrunich and Vishwanath [MV08] found that it is a continuous transition.

In the following two chapters, we present results of our numerical studies of the Néel-VBS transitions in JQ models [BDA10]. These results, together with recent work of Sandvik, establishes the continuous nature of the transitions in these JQ models beyond doubt and also reveals the presence of logarithmic violations of scaling at this critical point.

5

Antiferromagnet to valence bond solid transitions in staggered JQ models

As explained in the previous chapter, a key ingredient associated with the continuous transitions from a valence bond solid phase to an antiferromagnetic phase is the presence of a free spin half moment at the core of the vortex-like excitations of the valence bond solid ground state[LS04]. When such vortices condense to destroy the solid order, it naturally leads to an antiferromagnetic ordering. This implies that, if there are models analogous to the JQ models having low energy vortices without spinful cores in the solid phase, the considerations of deconfined criticality would not apply there. In such models, any possible transition from a valence bond solid phase to an antiferromagnet is expected to be first order in nature, conforming to Landau theory predictions.

In this chapter, we consider a few such models and provide evidence for first order Néel-VBS transitions in these models whenever increasing strength of the Q-term in the Hamiltonian could drive to such a transition. This indicates that the phase transitions in square lattice JQ models are special and supports a deconfined critical description of these transitions. The subsequent presentation is based on joint work with Arun Paramekanti and Kedar Damle (manuscript under preparation).

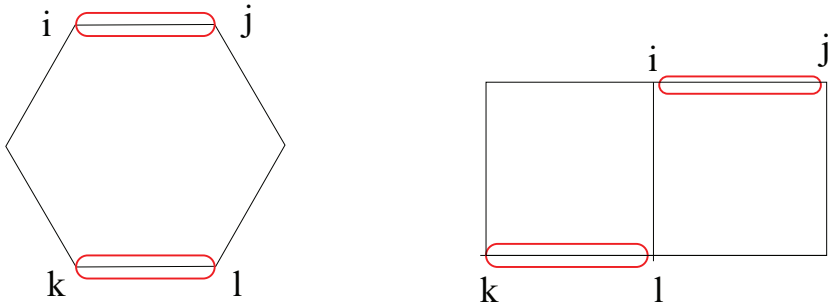

Figure 5.1: Four-spin operator $(P_{ij}P_{kl})$, consisting of product of singlet projectors P_{ij} and P_{kl}, in staggered JQ_2 model on honeycomb lattice (left) and square lattices (right). All possible operators related by lattice symmetry operations are present in the Hamiltonian.

5.1 Staggered JQ models: vortices with spinless cores

We find that a variation of Sandvik's JQ_2 model, where the favoured solid phase have staggered bond order instead of usual columnar order, allows for vortices with spinless cores in the solid phase. The Hamiltonian is similar to Sandvik's original JQ_2 model on square lattice, but the plaquettes are now made up of parallel bonds of neighbouring squares. (Recently this model have been studied by Sen et. al. [SS10], who using Monte Carlo techniques, has shown the presence of a first order Néel-VBS transition). We also consider similar staggered versions of the JQ_2 model on honeycomb lattice, where the plaquettes are made up of parallel bonds belonging to same or neighbouring hexagons. The plaquette operators for both of these models are illustrated in Fig. 5.1.

By analogy with standard JQ models [San07], these modified JQ models are expected to have a staggered valence bond solid ground state. Unlike standard columnar solid phase, in the staggered valence bond solid phase on square lattice, four domain walls can meet at the center of a square instead of a free spin - giving rise to a vortex that does not have a freespin at the core. Similarly in the staggered solid on honeycomb lattice, three domain walls may intersect at the center of a hexagon producing a spinless vortex core (see Fig.5.2). Note that in these models vortices with spinful cores are also allowed. But, the latter ones are likely to have higher energy cost associated with them, as a broken singlet should involve en-

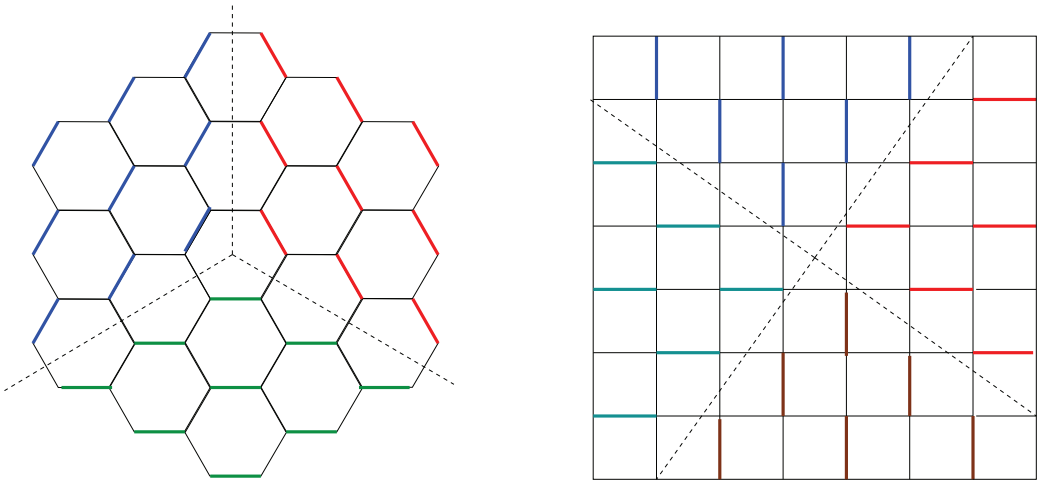

Figure 5.2: Cartoon of vortices in Staggered VB solid phase without any free spin at the vortex cores for honeycomb lattice and square lattice.

ergy penalty of the order of $\sim J$. If that is the case, then the transition away from staggered VBS solid would be driven by condensation of vortices with spinless cores. Thus, one may expect that for these variations of standard JQ models, the transition from a staggered VBS phase to a Néel ordered phase is a Landau-theory-like first order transition. It must be noted that, although the staggered Q-term is expected to drive a transition to a staggered valence bond solid phase, whether or not it does that can be decided by only by actual numerical simulations of these models. Our argument above only claims that if there are such transitions, they would be first order transitions.

5.2 Numerical results

We perform valence bond projector Monte Carlo study of these staggered JQ models on honeycomb and square lattices. Our aim is to investigate the nature of possible Néel-VBS transitions in these models. If such transitions do take place as coupling Q_2 is tuned and they are found to be of first order in nature without any ambiguity, that would clearly lend support to a deconfined quantum critical description, as argued by Senthil and Levin[LS04], of the transitions observed in Sandvik's JQ models [San10].

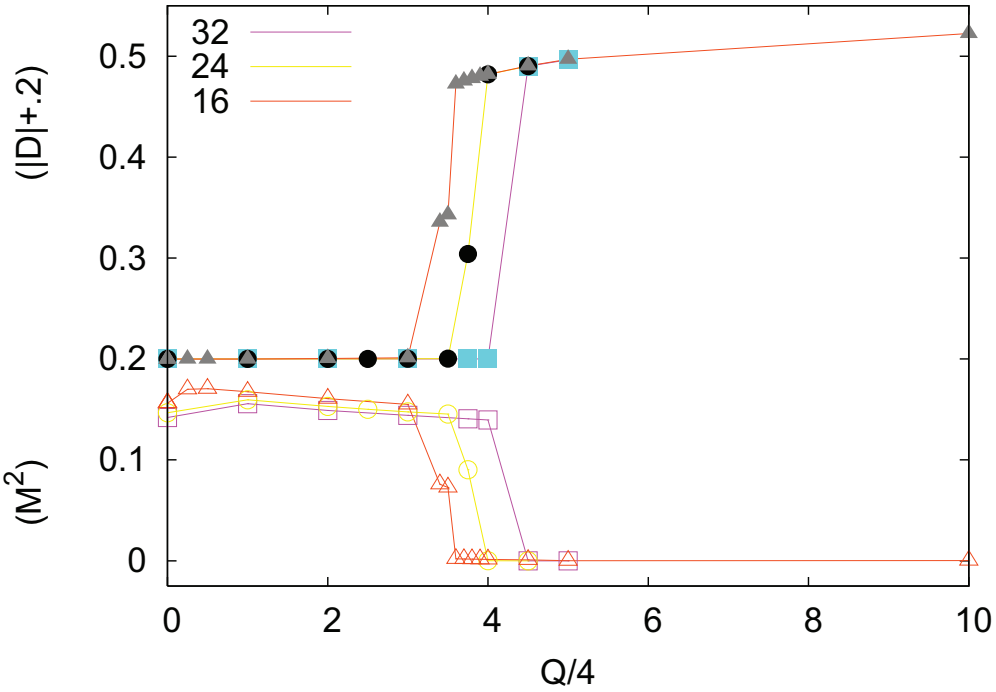

Figure 5.3: First order jump in order parameters C(l/2,l/2) and D(l/2,l/2) as $Q/4$ is varied for the Honeycomb model.

5.2.1 Measurements

Let us define $\rho_{(x,y);\mu} = \mathbf{S}_{(x,y)}.\mathbf{S}_{(x,y)+\hat{e_\mu}}$ with $\mu = 1, 2$ for vertical and horizontal bonds for the square lattice models (for honeycomb lattice models μ can take three values corresponding to three bond orientations). we measure following multi spin correlators to look for broken spin-symmetry and/or lattice translation symmetry,

$$C(L/2, L/2) = \langle \mathbf{S}_{(x,y)} \cdot \mathbf{S}_{(x,y)+(L/2,L/2)} \rangle, \text{ and} \tag{5.1}$$

$$D(L/2, L/2) = \langle \rho_{(x,y);\mu}\rho_{(x,y)+(L/2,L/2);\mu} - \rho_{(x,y);\mu}\rho_{(x,y)+(L/2,L/2);\nu} \rangle, \tag{5.2}$$

where $\mu \neq \nu$ in the second equation and L is the linear dimension of the system. For better statistics we average over all possible x, y, μ, and ν. In the presence of long range antiferromagnetic order, the asymptotic large size limit of $C(L/2, L/2)$ tends to a finite value, which is the square of staggered magnetisation and vanishes in absence of long range antiferromagnetic order. Similarly, $D(L/2, L/2)$, which is the difference of two

terms, serves as a order parameter for long range valence bond solid order. In a perfect staggered bond ordered solid, the first term gives finite contribution and the second term vanishes, as all the near neighbour valence bond singlets occupy one type of bonds. On the other hand, in the bond disordered phase all bond orientations are equally probable and the two terms cancel each other.

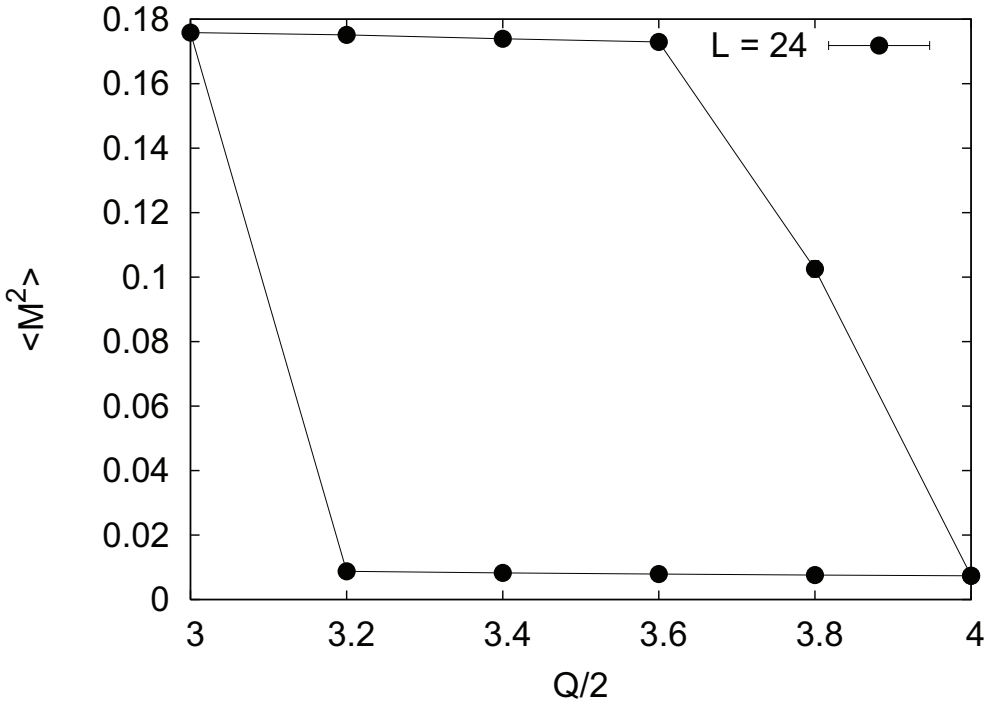

Figure 5.4: Hysteresis of $< \vec{M}^2 >$ around transition point for Honeycomb lattice JQ_2 model.

5.2.2 Results for honeycomb lattice models

We scan the phase diagram of honeycomb lattice JQ_2 models as a function of Q_2/J for systems with upto $2 \times 32 \times 32$ sites. Monte Carlo projection length of $6L^3$ is used to ensure convergence various observables to ground state expectation values. In this model, a transition form AF phase to VBS phase takes place as Q_2/J is increased, and at the transition point near $Q_2/2 \sim 3.5$, there are clear first order jumps in both the order parameters as shown in Fig.5.3. On closer look, the transition point, as

determined from the location of the jump, seems to be drifting with increasing system size. But, this is actually an artifact of the slowness of the code near the first order transition region at larger sizes. To get around this problem, we determine the transition point by locating the kink in the plot of energy as function of tuning parameter at smaller sizes, where there are no such issue of slowness of the code. As shown in Fig. 5.5, the energy per site shows a linear behaviour, but with slopes of the line changing discontinuously near the transition. This could be understood as a (avoided) level crossing taking place at the first order transition point. Identifying the crossing point of these two lines is a convenient way to determine the transition point [SS10]. Using this method, with data from three different system sizes $L = 12, 16$ and 24, we identify the transition to be $Q_c/2 = 3.2 \pm 0.1$.

First order transitions are associated with two coexisting free energy minima corresponding to the two phases. This leads to the appearance of hysteresis effects, as a configuration from one of the phases is evolved by tuning the coupling constant across the critical value at finite rate. For example, starting with a configuration deep in the solid phase, even at some Q less than Q_c the system remains stuck in the metastable solid state and vice versa. We present such a hysteresis plot for antiferromagnetic order parameter(Fig.5.4) near the transition to emphasise the first order nature of the transition.

We also obtain double peaked order parameter histogram near Q_c, which strengthens our claim of a first order transition. But it should be noted that due slowness of the code in the solid phase, we do not see multiple transitions between the two free energy minima corresponding to two phases. In the simulations for higher sizes near the transition point, the time taken for the system to tunnel between two equivalent ground states, is of the order of the total number of Monte Carlo steps.

In a variant of staggered JQ_2 model on honeycomb lattice, where parallel bonds from neighbouring hexagons make up the plaquette interactions, increasing Q_2 fails to destroy AF order. For this model, as shown in Fig. 5.7, there is no hint of a transition a transition for the range of Q_2 values studied. But as has been emphasized earlier, the presence of a Q term does not guarantee the existence of a valence bond solid phase so this lack of transition is not so unexpected.

5.2.3 Results for square lattice models

In our simulations on square lattice staggered JQ_2 model, we do not see any Néel-VBS transition. On the other hand in the JQ_3 model on this lattice we do see such a transition and this is again first order in nature. This is consistent with recent results obtained by Sen et. al.[SS10].

5.3 Summary

Thus, we see that in the solid phases of above staggered JQ models on the honeycomb and square lattice, vortices without any free spin at their cores are allowed. This coincides with the fact that whenever the Q term is able to drive a transition from an antiferromagnetic phase to a solid phase, there are clear first order discontinuities in both the order parameters. Hysteresis and double peaked order parameter histograms are obtained near such transition points, confirming the first order nature of these transitions. These results demonstrate that Néel-VBS transitions are generically first order in nature, which in line with Landau theory expectations, unless low energy vortices with spinful cores are present in the solid phase.

The above results clearly favour a deconfined quantum critical description of the Néel-VBS transition seen in Sandvik's JQ model [San10], where none of these signatures of an unambiguous first order transition have been observed.

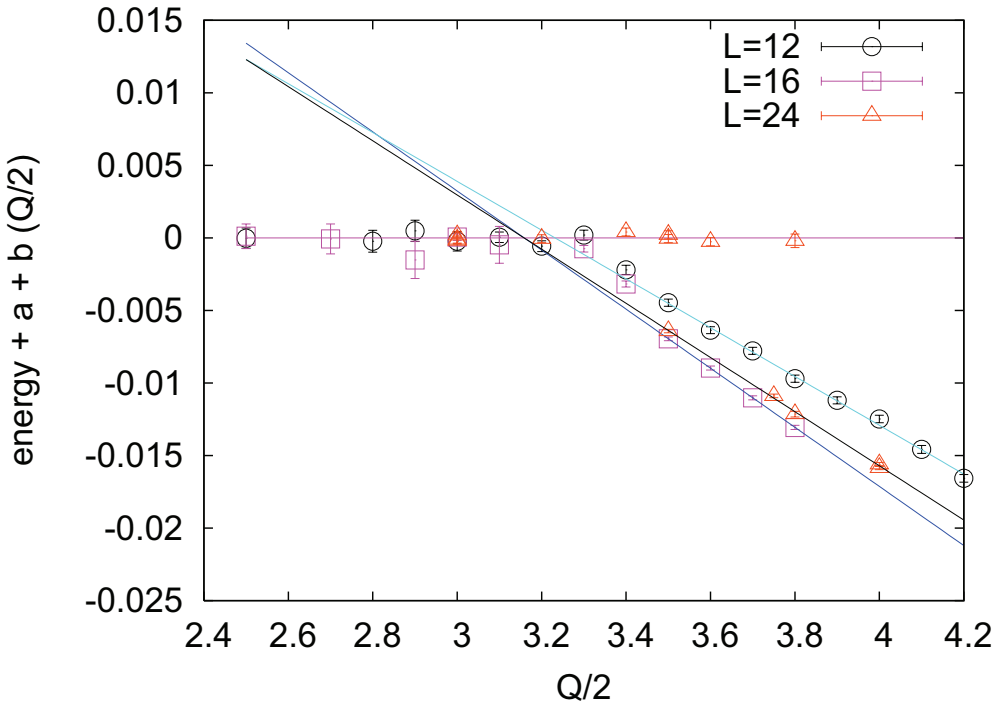

Figure 5.5: An avoided level crossing of the two competing candidate states for the ground state, showing up as a kink in the ground state energy of the honeycomb lattice staggered JQ_2 model, when plotted as a function of the tuning parameter Q. This serves as clear signature of the first order transition taking place in this model system. Note that energy difference from the fitted linear behaviour on the the antiferromagnetic side is plotted, not the absolute ground state energies on both sides - this is just to highlight the discontinuity of slopes of the two curves at the transition point. To obtain linear fits to energy values on the solid side, the data points at $Q/2 < 3.4$ have not been considered.

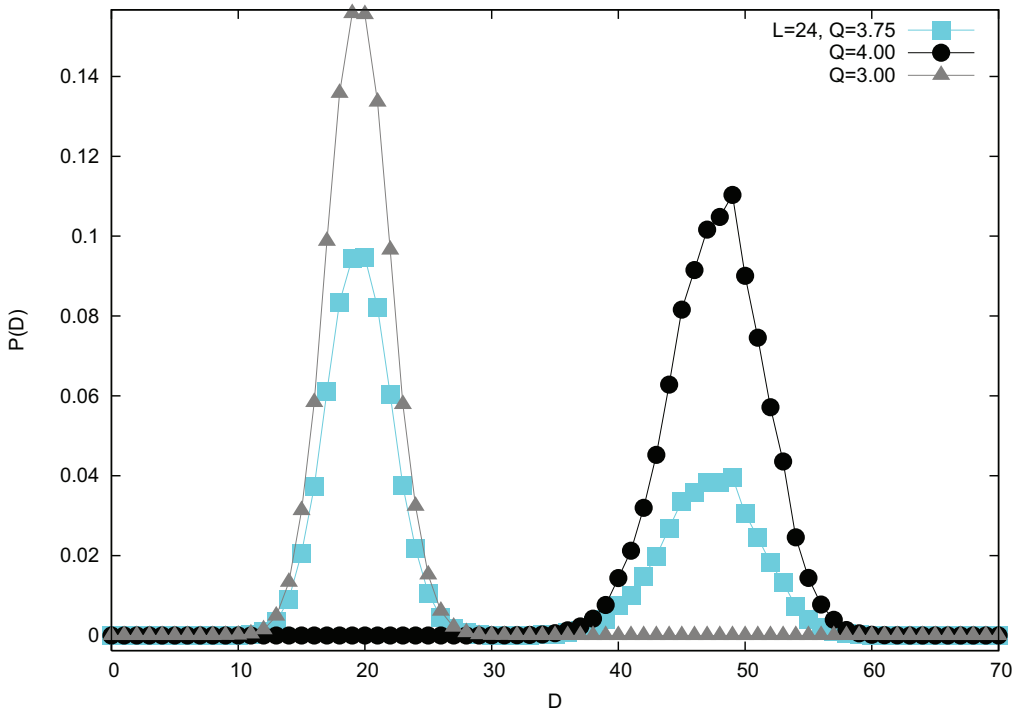

Figure 5.6: Histogram of valence-bond-solid order parameter D for L=24 at three different Q values for honeycomb lattice model. Presence of double peak structure at $Q/2 = 3.75$ indicates first order nature of transition.

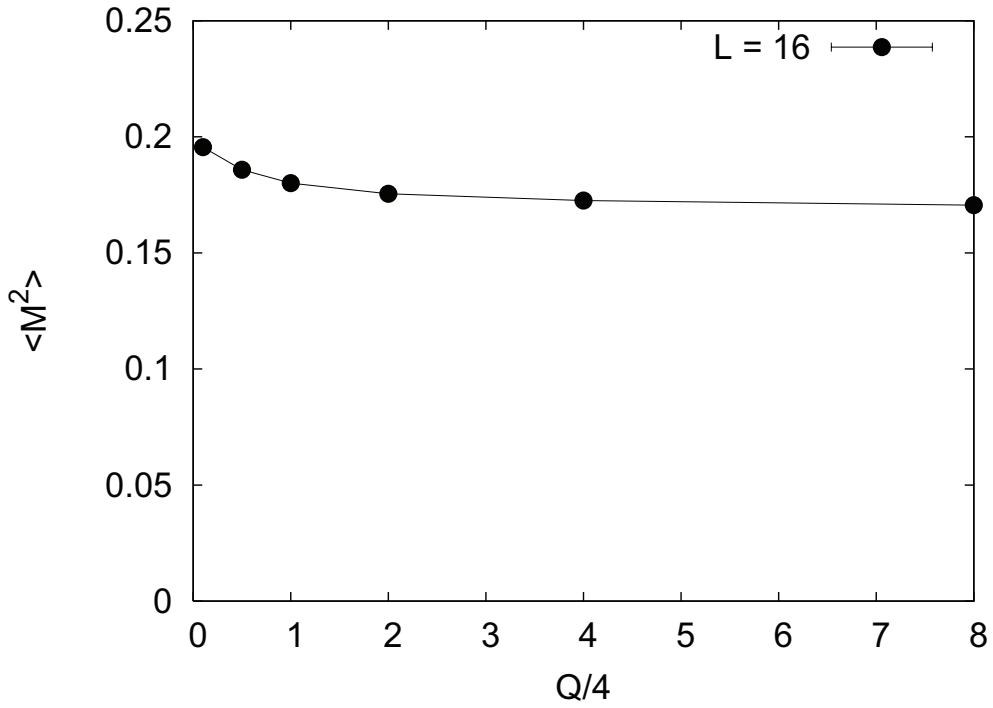

Figure 5.7: Order parameters $< \vec{M}^2 >$ as $Q/2$ is varied for the JQ_2 Honeycomb model with plaquettes made up of parallel bonds from neighbouring hexagons: no sign of a transition with increasing $Q/2$.

6

Impurity spin texture at a deconfined critical point

The effect of doped nonmagnetic impurities in a quantum spin-system has been the focus of many interesting experimental and theoretical studies. These includes measurements of impurity induced spin-textures in Heisenberg antiferromagnets, and various theoretical and numerical results on the properties of these textures at a quantum critical point. These studies establish that impurity effects can be a sensitive tool to understand various physical properties of spin-systems [ABGH09].

Motivated by this, we explore the the effects of a non-magnetic impurity in the JQ models [San07, LSK09], aiming to shed light on the precise nature of the controversial continuous transition in these models. We study the impurity induced spin textures in these models, and contrast it to the spin texture obtained at a conventional critical point. Our results [BDA10] provide important clues towards settling the issue of the nature of the transitions in the JQ models, as described in this chapter. The subsequent presentation is based on joint work with Kedar Damle and Fabien Alet ([BDA10], and manuscript under preparation).

6.1 Experimental motivation

With the advent of experimental probes like nuclear magnetic resonance and scanning tunneling microscopy etc., local spatial variations in observable quantities in the sample have become accessible to modern condensed matter experiments. This has led to the emergence of doped impurities as useful probe of the physical states of matter [ABGH09]. In these experiments, controlled quantities of impurities are added to the

pure sample, and the local effects of the impurity atom is studied at the microscopic level [TMEU97, BLA+09, DMB+04, OTI+99, BMA+99, BAM+01, MACM94, JFHac+00, TSHac99]. For example, Tedoldi et. al. [TSHac99] have studied the effect of the doped Mg atoms in an $S = 1$ Heisenberg spin chain compound Y_2BaNiO_5. Here the non-magnetic Mg^{2+} replaces $S = 1$ Ni^{2+}, and induces a local alternating spin texture around itself. The magnitude of this impurity texture decays exponentially as a function of the distance from the impurity atom. These induced spin polarisation in each of the Ni atom in turn causes shifts in the nuclear energy levels of near-neighbour ^{89}Y nucleus through hyperfine coupling. In an NMR experiment, these level shifts can be seen as additional resonance peaks, and the spin texture can be reconstructed from the measured values of the shifts of these peaks.

Motivated by these kinds of experiments, theorists too have taken up the problem of understanding the nature of the spin texture induced by a non-magnetic impurity [SBV99, MLRD97, ESAA07, KMMS08, PSV01, CP09, HSS07a]. As a result of these studies, it has become clear that the spin texture contains useful information about the nature of the pure system. For example, the universal scaling properties of the impurity texture at bulk critical points turn out to be very useful in order to understand the transitions better.

6.2 Scaling of impurity induced spin texture at conventional critical points

6.2.1 Scaling of impurity induced spin texture in real space

A non-magnetic impurity modifies the ground state of a spin systems, and induces both staggered and uniform spin textures around it. Though the detailed properties of the textures depend upon the nature of the ground states of the systems without any impurities, the impurity-induced spin texture $\Phi(\mathbf{r}) = \langle G|S^z(\mathbf{r})|G\rangle$ is expected to have a smooth uniform part $\Phi^u(\mathbf{r})$, and a Néel component $\Phi^n(\mathbf{r})$ that alternates in sign between the two sublattices of the square lattice. If the system is tuned to a critical point, both of these textures are expected to show universal scal-

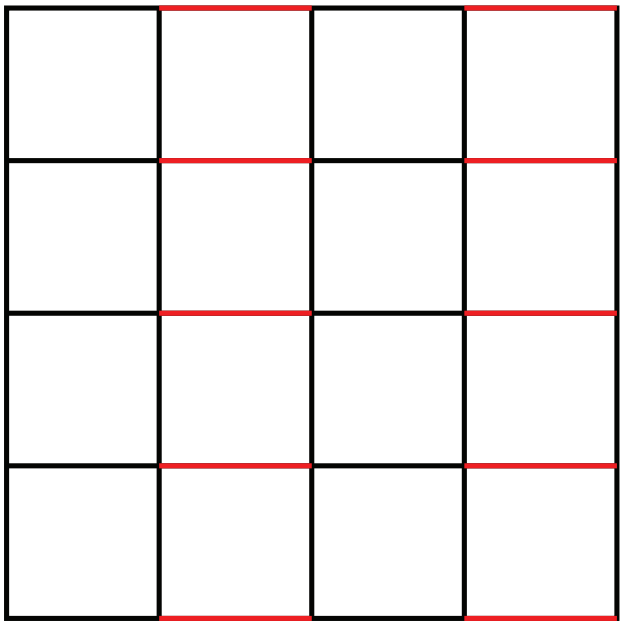

Figure 6.1: A cartoon of JJ' model Hamiltonian: The Black bonds correspond to exchange interaction strength J, and the red bond denotes interaction strength J'.

ing [HSS07b] properties,

$$\begin{aligned} \Phi^u(\mathbf{r}) &= \frac{1}{L^2} f^u(\mathbf{r}/L) \\ \Phi^n(\mathbf{r}) &= \frac{1}{L^{(1+\eta)/2}} f^n(\mathbf{r}/L), \end{aligned} \tag{6.1}$$

where $r >> 1$, η is the bulk correlation length exponent, and f^u (f^n) is the scaling function for the uniform (alternating) parts. This scaling behaviour has been validated by Hoglund et. al. [HSS07b] in a numerical study of a bilayer system at a continuous transition from a Néel ordered state to a gapped paramagnet. They define square frames around the impurity site, and calculate frame averaged uniform and alternate magnetisation as function of the perpendicular distance of the impurity site from the frame edges. Their data show that above scaling forms (6.1) describe very well the finite size properties of the frame averaged uniform and staggered spin textures.

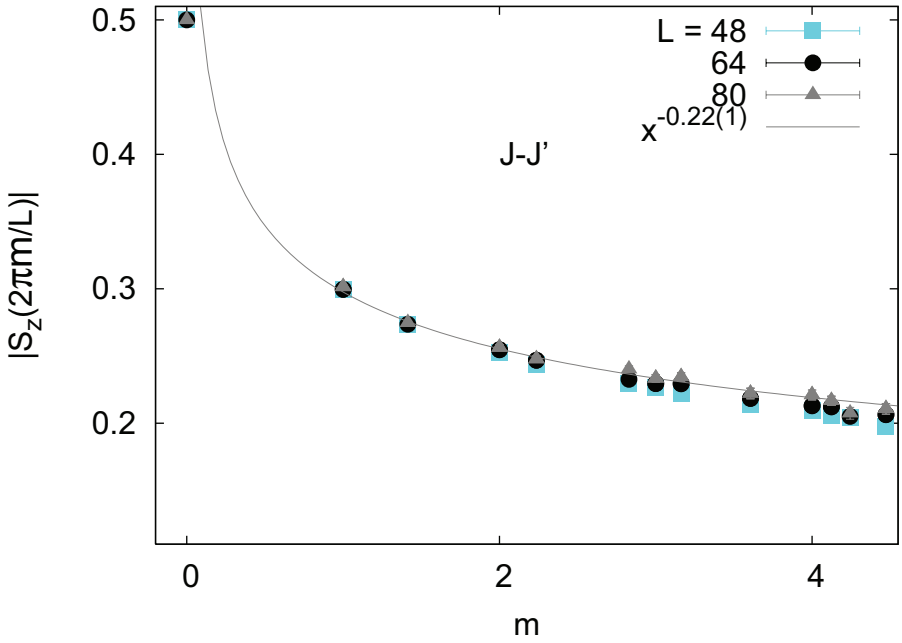

Figure 6.2: Scaling of the impurity induced spin texture at critical point of JJ' model near $\mathbf{k} = 0$.

6.2.2 Scaling of impurity induced spin texture in Fourier space

To investigate the scaling of the $S_{total} = 1/2$ ground state spin texture of a critical system with an impurity [BDA10], we look instead at the Fourier transform of the spin texture, $S_z(\mathbf{k}) = \sum_{\mathbf{r}} \Phi(\mathbf{r}) \exp(i\mathbf{k}\cdot\mathbf{r})$ (with $\mathbf{k} = 2\pi\mathbf{m}/L$ and $\mathbf{m} \equiv (m_x, m_y)$ with integers $m_{x/y} = 0, 1, \ldots L-1$). $S_z(\mathbf{k})$ is expected to have two peaks, one at $\mathbf{k} = 0$ with magnitude constrained to be $1/2$ (as we are in the $S_{total} = 1/2, S^z_{total} = 1/2$ sector), and the second one at $\mathbf{k} = \mathbf{Q} \equiv (\pi, \pi)$ due to the the tendency to Néel order. These observables are better motivated than the frame averaged quantities studied in Ref. [HSS07b], as these are in principle accessible in a magnetic scattering experiment. The scaling from (6.1), then implies the following scaling relations near these two Fourier peaks,

$$\begin{aligned} S_z(\mathbf{q}) &= g_0(L\mathbf{q}) \text{ for } |\mathbf{q}| \ll \pi/2 \\ S_z(\mathbf{Q}+\mathbf{q}) &= L^{(3-\eta)/2} g_{\mathbf{Q}}(L\mathbf{q}) \text{ for } |\mathbf{q} \ll \pi/2. \end{aligned} \tag{6.2}$$

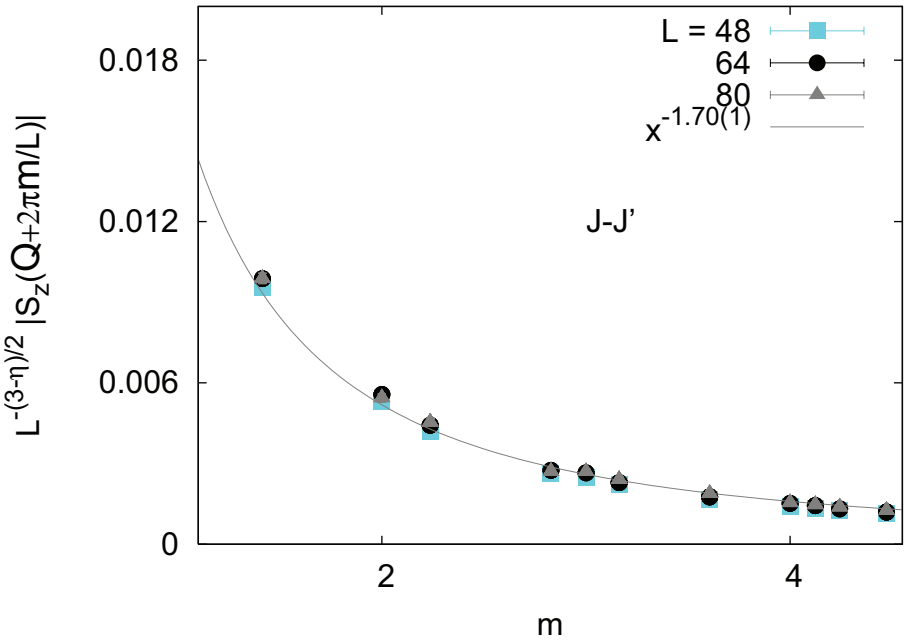

Figure 6.3: Scaling of the impurity induced spin texture at critical point of JJ' model near $\mathbf{k} = \mathbf{Q}$.

Also, from the asymptotic power law scaling form of the real space scaling functions in the limit $r << L$, it follows that, for small $L|\mathbf{q}|$, both $S_z(\mathbf{q})$ and $L^{-(3-\eta)/2}S_z(\mathbf{Q}+\mathbf{q})$ show universal power law behaviour controlled by a single impurity exponent η' [HSS07b]. In this limit, $S_z(\mathbf{q})$ goes as $(L|\mathbf{q}|)^{(-\eta'/2)}$, and $L^{-(3-\eta)/2}S_z(\mathbf{Q}+\mathbf{q})$ goes like $(L|\mathbf{q}|)^{-(3-\eta+\eta')/2}$.

First, we provide evidence that this Fourier space procedure captures very well the scaling properties of the impurity-spin-texture by exploring the impurity effects at a conventional Néel-paramagnet quantum critical point in the JJ' model. In this model, the exchange interaction on the alternate columns of horizontal bonds are strengthened to a value J', while on all remaining bonds the exchange is kept fixed at J (See Figure 6.1). As J'/J is tuned up from unity, the antiferromagnetically ordered system shows a continuous transition to a columnar VBS solid phase at $J'/J = 1.9096$ [WJ09]. This critical point is expected to belong to $O(3)$ universality class. We simulate this model at the bulk critical point, on periodic $L \times L$ lattices, with the central site removed. Our system sizes range from $L = 48$ to 96, and we look at the $S_{total} = 1/2, S^z_{total} = 1/2$ ground state spin texture. Note that the scaling collapse data given here

is obtained by eye-estimation. A better method would be to use some automated numerical procedure to obtain the best possible scaling collapse, which would also give an quantitative handle on the goodness of the collapse obtained.

As expected, we obtain nice scaling collapse near the Fourier peaks at $\mathbf{k} = 0$ and $\mathbf{k} = \mathbf{Q}$. Figures 6.2, and 6.3 shows this scaling collapse, obtained using the known values of the critical exponents in this $O(3)$ transition [HSS07b]. It should also be noted that the estimated impurity scaling exponent η', obtained independently by looking at the asymptotic power law behaviour of the impurity texture at both $\mathbf{k} = 0$ and $\mathbf{k} = \mathbf{Q}$, is consistent with that obtained by Hoglund et.al. in their study of the bilayer model [HSS07b].

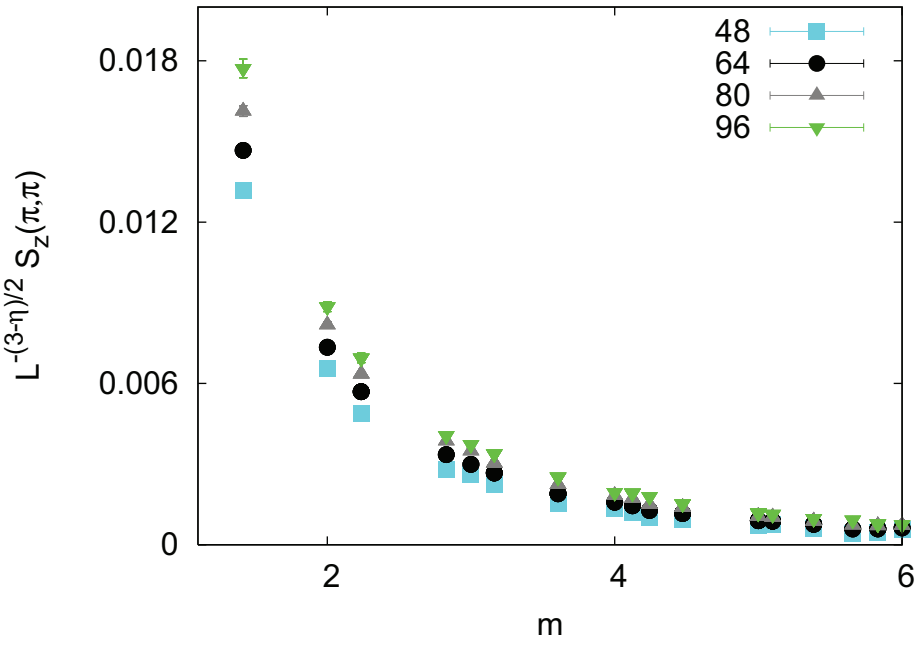

Figure 6.4: Attempted scaling collapse of $S_z(\mathbf{k})$ near $\mathbf{k} = \mathbf{Q}$ at the Néel-VBS transition, with $l_{\mathbf{Q}} = 0.75 \pm 0.2$ for the JQ_2 model.

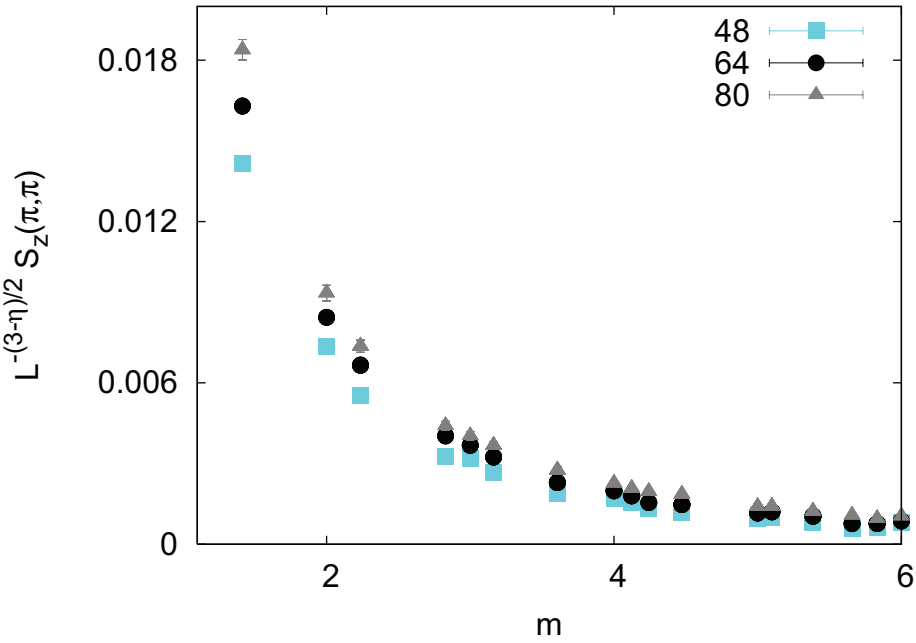

Figure 6.5: Attempted scaling collapse of $S_z(\mathbf{k})$ near $\mathbf{k} = \mathbf{Q}$ at the Néel-VBS transition, with $l_{\mathbf{Q}} = 1.5 \pm 0.5$ for the JQ_3 model.

6.3 Scaling of impurity induced spin texture at a deconfined critical point

6.3.1 Failure of standard scaling forms for impurity textures in the JQ models

The first indications that standard scaling does not work at these Néel-VBS transitions in the JQ-models, come from the behaviour of computed values of $|S_z(\mathbf{q})|$ for different system sizes, as shown in Figures 6.4,6.5,6.6,6.7 (left panels) for $\mathbf{q} = 2\pi\mathbf{m}/L$ with $|\mathbf{m}| \ll L/2$, that is, in the vicinity of the peak at $\mathbf{q} = \mathbf{0}$. In this figure, we have concentrated on data for $|\mathbf{m}| \leq L/12$ and averaged over all $\mathbf{m}$ corresponding to a given $|\mathbf{m}|$ for better statistics . Larger values of L are seen to yield a systematically larger value of $|S_z(\mathbf{q})|$ at the same $|\mathbf{m}|$. This behaviour at the Néel-VBS transitions is in clear violation of the scaling form Eq. 6.2; this should be contrasted with the excellent scaling observed at the conventional Néel-paramagnet critical point of the JJ' model (Fig. 6.2). Given

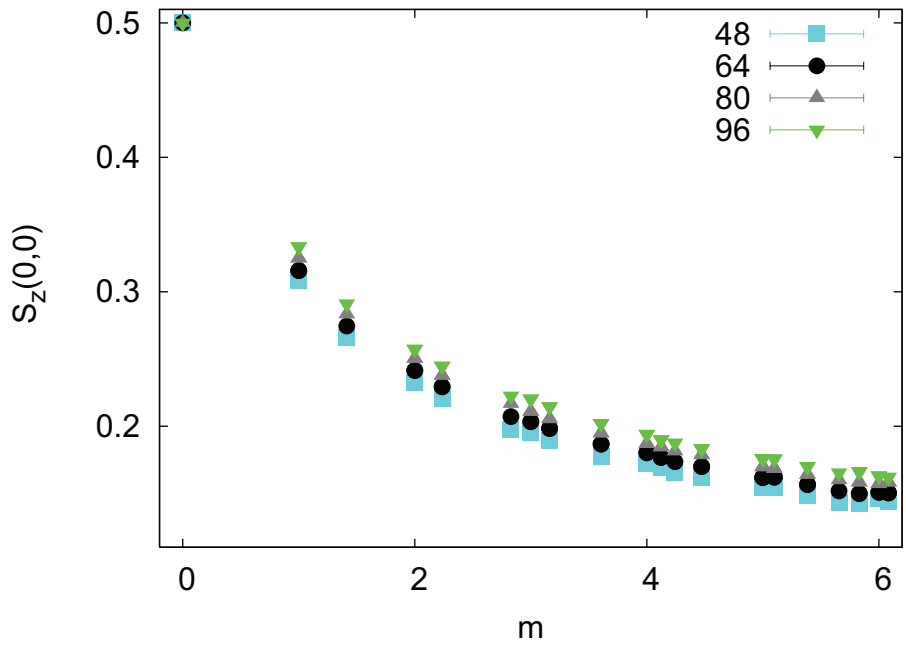

Figure 6.6: Attempted scaling collapse of $S_z(\mathbf{k})$ near $\mathbf{k} = \mathbf{0}$ at the Néel-VBS transition, with $l_{\mathbf{Q}} = 0.75 \pm 0.2$ for the JQ_2 model.

the unbiased nature of this test of scaling, which has already been validated for JJ' model, clearly this provides strong evidence for violation of impurity scaling properties at these Néel-VBS transitions in the JQ_2 and JQ_3 models.

Next, we analyse the Bragg peak at the antiferromagnetic wavevector, $\mathbf{k} = \mathbf{Q}$, focusing on the L dependence at the Néel-VBS transition points. We find that the peaks values obey the power-law scaling $|S_z(\mathbf{Q})| \sim L^{(3-\eta)/2}$ quite well for both models, with the anomalous exponents $\eta_{JQ_3} \approx 0.33$ and $\eta_{JQ_2} \approx 0.35$ taken from Ref [LSK09, MK08]. Our results for the $JJ^{'}$ model are also consistent with the power-law scaling $|S_z(\mathbf{Q})| \sim L^{(3-\eta)/2}$ with the known value of $\eta \approx 0.04$ for the Néel-paramagnet QPT [HSS07b]. However, violations of impurity scaling in the staggered component of the texture at the Néel-VBS transitions become evident when one tests for scaling collapse at $\mathbf{k} = \mathbf{Q} + 2\pi\mathbf{m}/L$ with $|\mathbf{m}| \ll L/2$. In a manner similar to the scaling violation seen near $\mathbf{k} = \mathbf{0}$, larger L give larger values of $|S_z(\mathbf{k})|$ for the same non-zero $|\mathbf{m}|$. Again, this should be contrasted with the excellent scaling collapse found at the Néel-paramagnet QPT of the $JJ^{'}$ model (Figure 6.3).

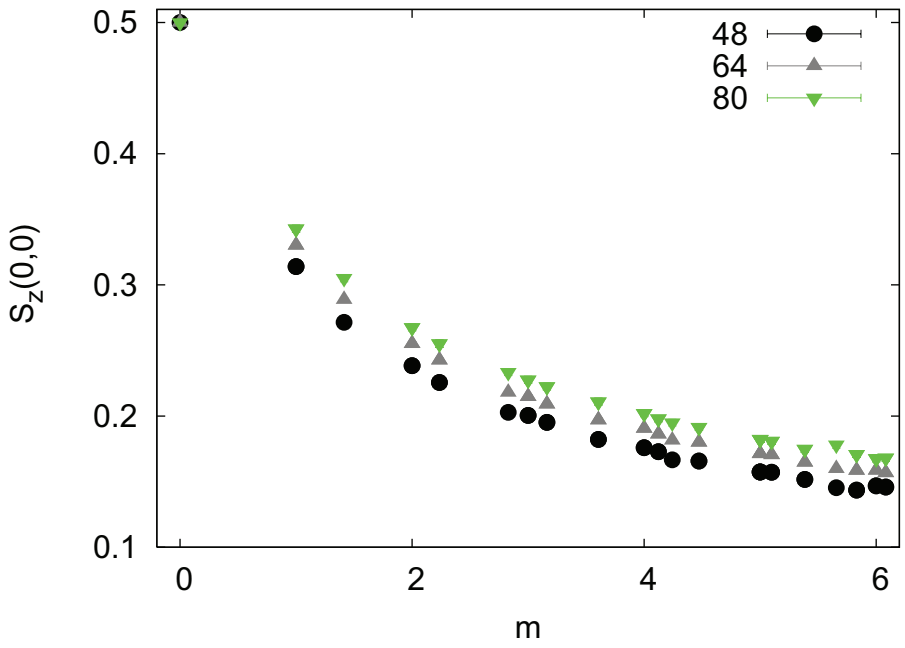

Figure 6.7: Attempted scaling collapse of $S_z(\mathbf{k})$ near $\mathbf{k} = \mathbf{0}$ at the Néel-VBS transition, with $l_{\mathbf{Q}} = 1.5 \pm 0.5$ for the JQ_3 model.

It may be argued that these scaling violations described above are possibly due to conventional finite-size corrections. To investigate this issue, below we try to fit these scaling violations to standard finite size correction forms. Since the scaling functions $g_{0/\mathbf{Q}}$ have a dimensionless argument $\mathbf{m}$, the possible finite-size corrections should be incorporated by modifying their argument as follows, $\mathbf{m}(1 + (l_{0/\mathbf{Q}}/L)^p)$. In this modified argument of the scaling functions, the positive power p controls the approach to the asymptotic scaling regime when L becomes much larger than the microscopic length scale $l_{0/\mathbf{Q}}$. Next, we attempt to collapse the data for various sizes near the Fourier peaks using this particular from of finite-size corrections, by varying both l_0 and p. We find that this fit only works for unphysically large best-fit length scales $l^p_{0/\mathbf{Q}} \gtrsim 100$. And the powers p takes the values 0.2—0.6, depending on which JQ model and which peak. For example, in JQ_2 model, $p = 0.2$ works well for both the peaks (see Figures 6.8, 6.9). These large values of the best-fit length scale clearly indicates that the scaling argument has the form $\mathbf{m}/L^p$ for both of these models, rather than the standard finite scaling form $\mathbf{m}(1 + (l_{0/\mathbf{Q}}/L)^p)$.

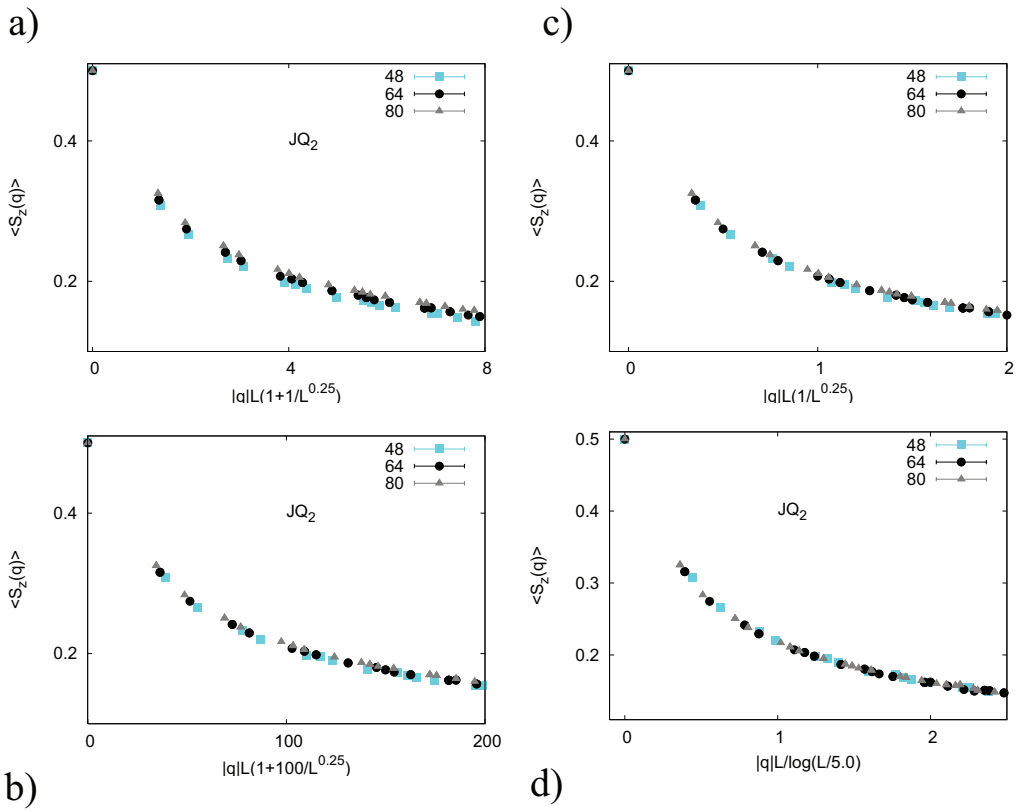

Figure 6.8: Attempt to explain lack of scaling of $S_z(\mathbf{k})$ near $\mathbf{k} = \mathbf{0}$ at the Néel-VBS transition for the JQ_2 model as finite size effects.

6.3.2 Logarithmic violations of impurity scaling properties in the JQ models

We are thus led to a scaling argument of the form $\mathbf{m}/L^p$ with small $p \sim 0.2$—0.6 to obtain good scaling collapse. This kind of scaling form has no known basis in the theory of phase transitions. But it should be noted that for such small p, this form is essentially indistinguishable from logarithmic violations of impurity scaling, with scaling argument $\mathbf{m}/\log(L/l_{0/\mathbf{Q}})$. Such logarithmic violations are known to arise as consequences of marginally irrelevant perturbations of the critical fixed point. In fact, recent work of Sandvik [San10] has seen other signatures of such logarithmic violations at the bulk Neel-VBS transitions in impurity-free periodic systems. We therefore consider the following modified scaling

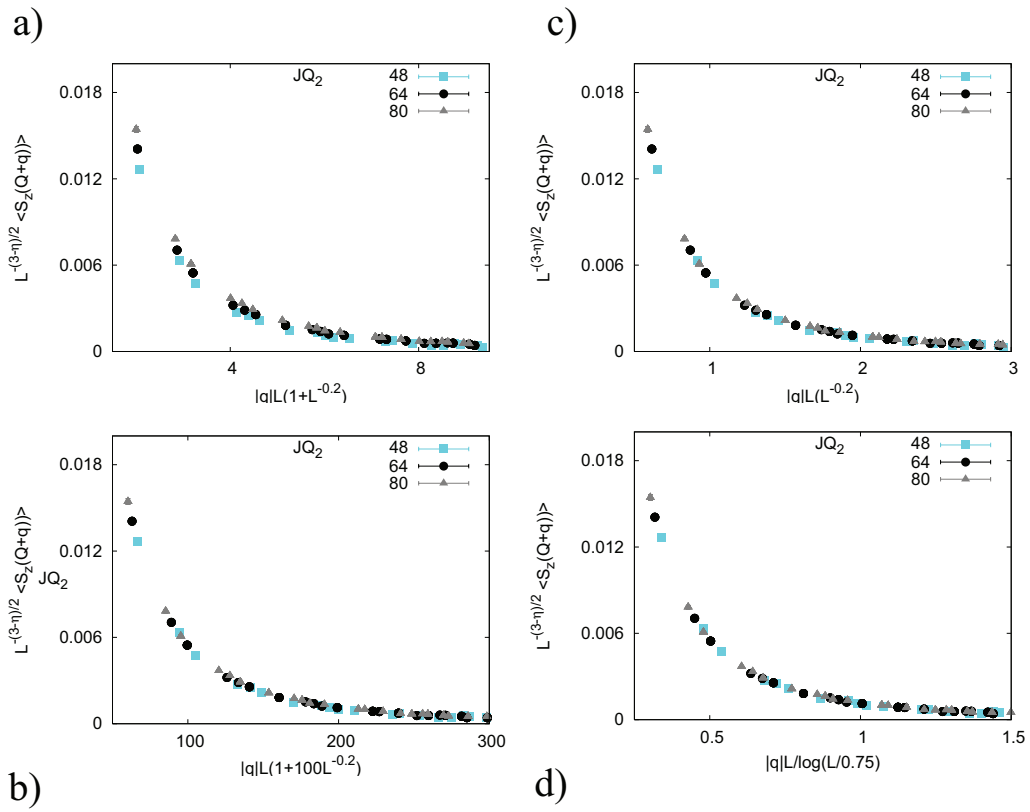

Figure 6.9: Attempt to explain lack of scaling of $S_z(\mathbf{k})$ near $\mathbf{k} = \mathbf{Q}$ at the Néel-VBS transition for the JQ_2 model as finite size effects.

form to describe the computed spin texture (for $|\mathbf{q}| \ll \pi/2$),

$$\begin{aligned} S_z(\mathbf{q}) &= g_0(L\mathbf{q}/\log(L/l_0)) \\ S_z(\mathbf{Q}+\mathbf{q}) &= L^{(3-\eta)/2} g_{\mathbf{Q}}(L\mathbf{q}/\log(L/l_{\mathbf{Q}})), \end{aligned} \tag{6.3}$$

where l_0 and $l_{\mathbf{Q}}$ now represent the additional non-universal length scale introduced by the slow vanishing of some marginally irrelevant operators. As is clear from Figures 6.10 and 6.11, this modified scaling law works extremely well and fits the violations of standard critical scaling seen above.

This leads to the conclusion that, although the Néel-VBS transition is continuous, the critical theory has logarithmic violations of scaling. The proposed field theory to describe these deconfined critical transitions [SBS+04], does not explain the presence of the logarithmic violations of impurity scaling in JQ models as seen above. Thus, logarithmic

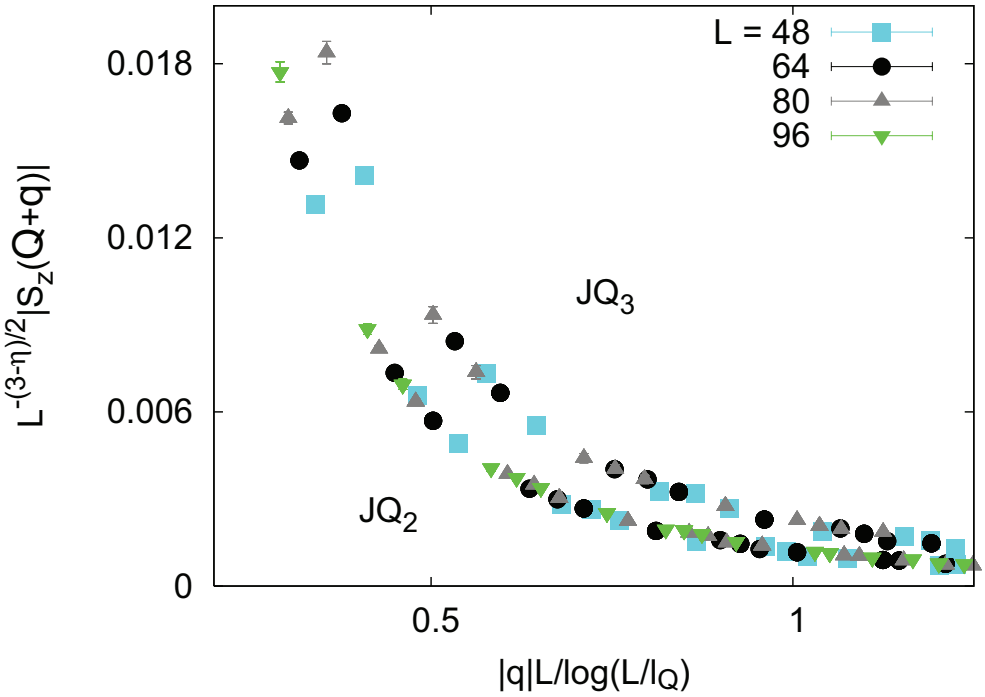

Figure 6.10: Logarithmically modified scaling collapse of $S_z(\mathbf{k})$ near $\mathbf{k} = \mathbf{Q}$ at the Néel-VBS transition, with $l_0 = 5 \pm 1$ ($l_0 = 12 \pm 1$) for the JQ_2 (JQ_3) model.

violations of critical scaling of impurity properties reported here, together with the logarithmic corrections to scaling in the bulk critical properties of JQ models as reported by Sandvik [San10], demand serious rethinking of the standard field theoretic descriptions of these continuous transitions. This conclusion also underlines the utility of impurity physics as a probe of complex strongly-correlated states of many-body systems.

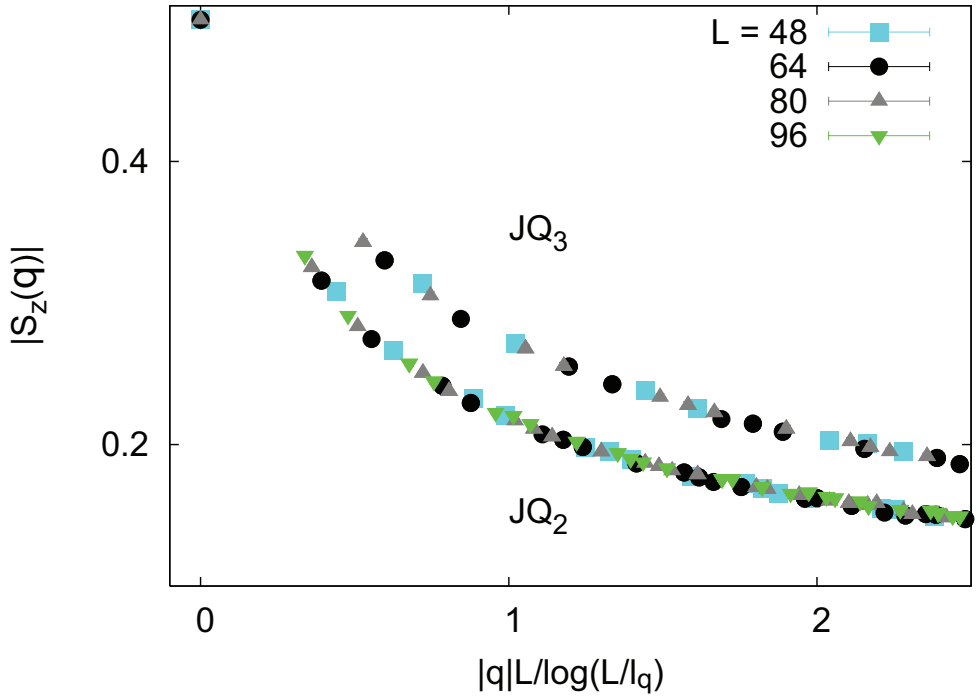

Figure 6.11: Logarithmically modified scaling collapse of $S_z(\mathbf{k})$ near $\mathbf{k} = \mathbf{0}$ at the Néel-VBS transition, with $l_0 = 5 \pm 1$ ($l_0 = 12 \pm 1$) for the JQ_2 (JQ_3) model.

6.4 Scaling of impurity induced spin texture in a $SU(3)$ symmetric generalisation of the JQ_2 model

6.4.1 The model

It is known that a $SU(N)$ symmetric generalisation of the Heisenberg model shows a Néel-VBS transition as N is tuned [RS89]. In fact, for a N value of 4 or less the ground state is antiferromagnetically ordered, while for $N = 5$ and above, it is a lattice symmetry broken valence bond solid [KT07, BAMC09]. The generalised Heisenberg model is given by,

$$H_{SU(N)} = J/N \sum_{\langle ij \rangle} \mathbf{S}_i^{\alpha\beta} \mathbf{S}_j^{\alpha\beta}, \tag{6.4}$$

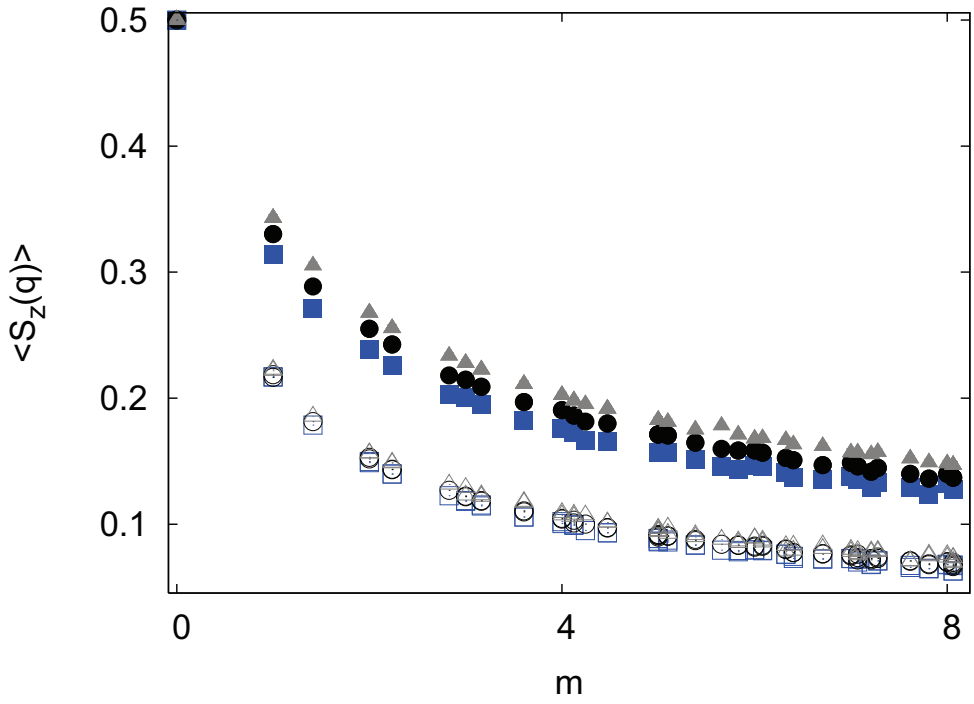

Figure 6.12: Scaling of the impurity induced spin texture at the critical point of $SU(3)$ symmetric JQ_2 model near $\mathbf{k} = 0$(open symbols) for system sizes L=48 64, 80. Similar data at the $SU(2)$ JQ_3 critical point is also presented (solid symbols) for comparison (Note that for the $SU(3)$ data shown have been multiplied by a factor of $1/2$ to enable a fair comparison with $S^z_{total} = 1/2$ $SU(2)$ data).

where $\mathbf{S}_i^{\alpha\beta}$ is the generator of the $SU(N)$ algebra, with $\alpha, \beta = 1, \cdots, N$. The spins on A-sublattice are in the fundamental representation, and on B-sublattice spins are the $SU(N)$ conjugates of those on A-sublattice. The same model can be write as,

$$H_{SU(N)} = -J \sum_{\langle ij \rangle} C_{ij} + 2JL^2/N^2, \tag{6.5}$$

where, $C_{ij} = 1/N^2 - \mathbf{S}_i^{\alpha\beta}\mathbf{S}_j^{\alpha\beta}/N$, is the $SU(N)$ generalisation of singlet projectors.

Lou et. al. [LSK09] have considered the $SU(N)$ generalisation of the JQ_2 model on square lattice with $N = 3, 4$. They have shown that in these models, a continuous Néel-VBS transition takes place as Q/N is tuned

up(Note that for $N \geq 5$, the ground state is a VB solid even at $Q = 0$). Below, we study impurity effects at the continuous transition observed in the $SU(3)$ symmetric JQ_2 model.

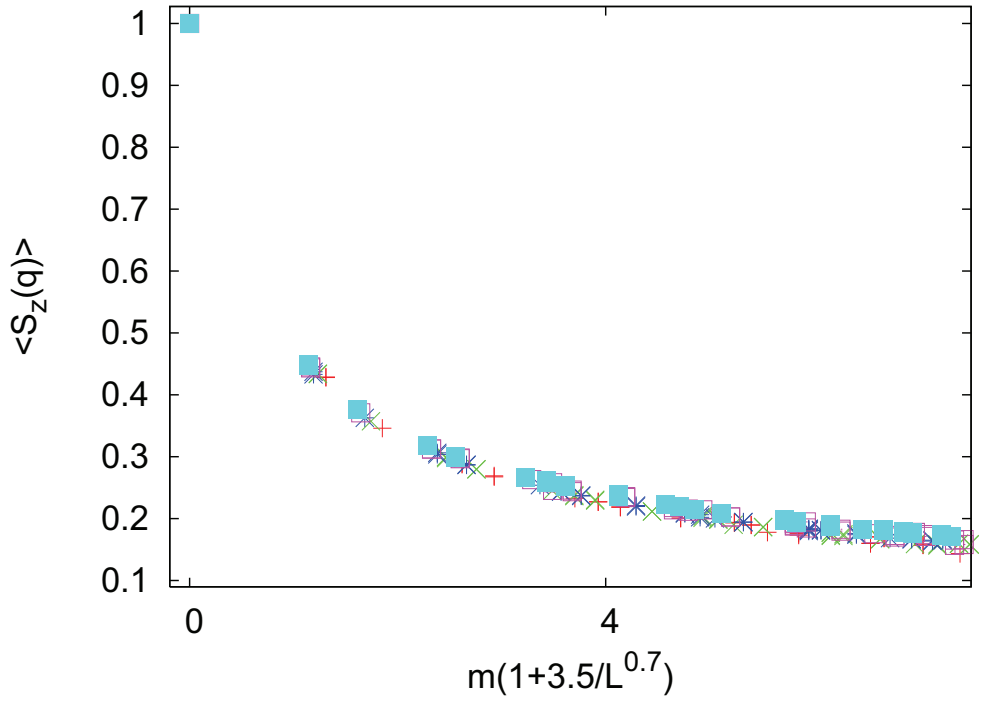

Figure 6.13: Attempted scaling collapse of $S_z(\mathbf{k})$ near $\mathbf{k} = \mathbf{0}$ at the Néel-VBS transition for the JQ_2 ($SU(3)$) model, assuming finite size corrections as described in the text.

6.4.2 Simulations

The singlet sector valence bond method with loop updates can readily be generalised to handle these $SU(N)$ symmetric models. In this context, it is convenient to appeal to the alternative description of these $SU(N)$ models as $SU(2)$ systems with spin $S = (N-1)/2$, with interactions in the form of appropriate projectors [BAMC09]. For example, in the $SU(3)$ case, the bipartite projector looks like, $\frac{1}{3}\left((\mathbf{S}_i.\mathbf{S}_j)^2 - 1\right)$ with $S = 1$. Here, the bipartite valence bond basis spans only the $SU(3)$ symmetric subspace of the full singlet sector and a valence bond denotes the state, $1/\sqrt{3}\left(|-1,1\rangle - |0,0\rangle + |1,-1\rangle\right)$. The only changes in the algorithm is

that each VB loop now has three orientations and the reconnection amplitude is $1/3$ (in general, for a $SU(N)$ model, it is $1/N$). Clearly, the generalisation of the $S_{total} = 1/2$ $SU(2)$ algorithm is also possible, only concern being whether or not the ground state lies in the subspace spanned by extended valence bond basis with an extra free spin. We have implemented this algorithm, and checked that for small system sizes it gives the right ground state properties when compared with exact results. We use this method to compute the impurity induced spin texture at the critical point of the above $S = 1$ JQ_2 model [LSK09] in the $S_{total} = 1, S^z_{total} = +1$ sector.

6.4.3 Results

In this section, to investigate the scaling properties of the spin texture, we concentrate on the peak near $\mathbf{k} = \mathbf{0}$, as here, there are no anomalous scaling exponent involved in the scaling form. In Fig. 6.12, we can see that $S_z(\mathbf{k})$ near $\mathbf{k} = \mathbf{0}$ shows much better scaling collapse, compared to what was seen in the $SU(2)$ JQ_3 model impurity textures. This $SU(2)$ spin texture near $\mathbf{k} = \mathbf{0}$, is also plotted in the same plot for ease of comparison. Clearly, the conventional scaling ansatz 6.2 works much better in the $SU(3)$ case.

But on closer look, small systematic deviations from scaling are visible even for the $SU(3)$ impurity texture (Fig. 6.12). It turns out that, this can be accounted for by conventional finite size effects. To establish that, as before, we modify the argument of the scaling from 6.2 to $\mathbf{m}(1 + (l_0/L)^p)$, and try to obtain values of l_0 and p that give us good collapse. As shown in Fig. 6.13, a nice collapse is obtained using $l_0^p \sim 3.5$ and $p \sim 0.7$. When contrasted with unphysically large ($\gtrsim 100$) values of l_0 obtained in the corresponding $SU(2)$ case, the small but systematic deviations from scaling of impurity spin textures in this $SU(3)$ symmetric model seems to be a conventional finite size effect. So we do not need to look for a more complicated explanation in the from of logarithmic violations to scaling caused by some unknown marginal perturbation present in the effective field theory description. This result, in fact, serves as a hint that the related perturbations do not remain marginal as we go from $N = 2$ to $N = 3$ and become irrelevant for $N > 2$, thereby restoring conventional scaling.

6.5 Summary

We have used the scaling properties of non-magnetic impurity induced spin textures to probe the nature of the Néel-VBS phase transition in the JQ models. Analysing the Fourier transform of the measured spin texture, we identified logarithmic violations of critical scaling at these continuous transitions. This result is in sharp contrast to the good scaling collapse of the similar Fourier transformed textures at the conventional critical transition of the JJ' model. These logarithmic violations of scaling indicates the presence of marginal perturbations in the critical field theory describing these transitions, which is not explained by the current theory of deconfined criticality. We also establish, by looking at the spin texture at the analogous Néel-VBS transition point in a $SU(3)$ generalisation of the JQ_2 model, that the postulate of the presence of marginal operators is not essential to explain the scaling properties of the spin texture.

7 Conclusions

In this thesis, we have numerically studied the ground state properties of model quantum magnets. we have generalised the singlet sector valence bond projector Monte Carlo technique [San07] to some cases where the ground state lies in the total spin ($S_{total} = 1/2$) sector[BD10], e.g., ground state of a $S = 1/2$ Heisenberg antiferromagnet consisting of odd number of spins. This extension is very useful in modeling many experimental situations, for example, the effects of doped nonmagnetic impurities in antiferromagnetic parent compounds. we have applied this technique to study the effect of finite size and open edges in $S = 1/2$ Heisenberg antiferromagnets on an $L \times L$ square lattice with L odd. We also investigate the scaling of impurity induced spin texture at bulk quantum critical points for various models. In our study of impurity effects in the JQ models [BDA10], which are supposed to show a deconfined quantum critical transition form an antiferromagnet to a valence bond solid state, we identified logarithmic violations to critical scaling. We have also shown that in a $SU(3)$ generalisation of the JQ_2 model, the impurity induce spin textures follow standard scaling laws. These results provide important clues towards a better theoretical understanding of deconfined critical phenomena. We also study the nature of the transitions in staggered versions of original JQ models and establish the first order nature of antiferromagnet to valence bond solid transitions in these models - these results support a deconfined quantum critical description of the continuous transitions in the JQ models.

Bibliography

[AAC+07] A.F. Albuquerque, F. Alet, P. Corboz, P. Dayal, A. Feiguin, S. Fuchs, L. Gamper, E. Gull, S. GÂÿrtler, A. Honecker, R. Igarashi, M. KËĘrner, A. Kozhevnikov, A. LâĂřuchli, S.R. Manmana, M. Matsumoto, I.P. McCulloch, F. Michel, R.M. Noack, G. Pawlowski, L. Pollet, T. Pruschke, U. SchollwËĘck, S. Todo, S. Trebst, M. Troyer, P. Werner, and S. Wessel, *The ALPS project release 1.3: Open-source software for strongly correlated systems*, Journal of Magnetism and Magnetic Materials **310** (2007), no. 2, Part 2, 1187 – 1193, Proceedings of the 17th International Conference on Magnetism, The International Conference on Magnetism. 12

[ABGH09] H. Alloul, J. Bobroff, M. Gabay, and P. J. Hirschfeld, *Defects in correlated metals and superconductors*, Rev. Mod. Phys. **81** (2009), no. 1, 45. 14, 15, 33, 57

[AM03] N. W. Ashcroft and N. D. Mermin, *Solid state physics*, international student ed., ch. 10, p. 175, Thomson, Singapore, 2003. 8

[Aue94a] A. Auerbach, *Interacting electrons and quantum magnetism*, second ed., ch. 3, p. 31, Springer-Verlag, New York, 1994. 9

[Aue94b] ———, *Interacting electrons and quantum magnetism*, second ed., ch. 11, p. 113, Springer-Verlag, New York, 1994. 10

[BAM+01] J. Bobroff, H. Alloul, W. A. MacFarlane, P. Mendels, N. Blanchard, G. Collin, and J.-F. Marucco, *Persistence of Li Induced Kondo Moments in the Superconducting State of Cuprates*, Phys. Rev. Lett. **86** (2001), no. 18, 4116–4119. 58

[BAMC09] K. S. D. Beach, Fabien Alet, Matthieu Mambrini, and Sylvain Capponi, *$SU(N)$ Heisenberg model on the square lattice: A continuous- N quantum Monte Carlo study*, Phys. Rev. B **80** (2009), no. 18, 184401. 69, 71

[BD10] Argha Banerjee and Kedar Damle, *Generalization of the singlet sector valence-bond loop algorithm to antiferromagnetic ground*

states with total spin S tot = 1/2, Journal of Statistical Mechanics: Theory and Experiment **2010** (2010), no. 08, P08017. 15, 17, 21, 34, 75

[BDA10] Argha Banerjee, Kedar Damle, and Fabien Alet, *Impurity spin texture at a deconfined quantum critical point*, Phys. Rev. B **82** (2010), no. 15, 155139. 15, 45, 57, 60, 75

[BLA+09] J. Bobroff, N. Laflorencie, L. K. Alexander, A. V. Mahajan, B. Koteswararao, and P. Mendels, *Impurity-Induced Magnetic Order in Low-Dimensional Spin-Gapped Materials*, Phys. Rev. Lett. **103** (2009), no. 4, 047201. 58

[BMA+99] J. Bobroff, W. A. MacFarlane, H. Alloul, P. Mendels, N. Blanchard, G. Collin, and J.-F. Marucco, *Spinless Impurities in High-T_c Cuprates: Kondo-Like Behavior*, Phys. Rev. Lett. **83** (1999), no. 21, 4381–4384. 58

[BS06] K.S.D. Beach and Anders W. Sandvik, *Some formal results for the valence bond basis*, Nuclear Physics B **750** (2006), no. 3, 142 – 178. 17, 18, 19, 20, 22, 25, 27, 28, 29

[CL98] P. M. Chaikin and T. C. Lubensky, *Principles of condensed matter physics*, first paperback ed., ch. 4, New Delhi, 1998. 39, 41

[CP09] Manuela Capello and Didier Poilblanc, *Many-body calculation of the spatial extent of the wave function of a nonmagnetic impurity in a d -wave high-temperature superconductor using the $t-J$ model*, Phys. Rev. B **79** (2009), no. 22, 224507. 58

[CRT+95] M. Corti, A. Rigamonti, F. Tabak, P. Carretta, F. Licci, and L. Raffo, *^{139}La NQR relaxation and μSR study of Zn-doping effects in La_2CuO_4*, Phys. Rev. B **52** (1995), no. 6, 4226–4236. 33

[Dag94] Elbio Dagotto, *Correlated electrons in high-temperature superconductors*, Rev. Mod. Phys. **66** (1994), no. 3, 763–840. 9

[DMB+04] J. Das, A. V. Mahajan, J. Bobroff, H. Alloul, F. Alet, and E. S. Sørensen, *Comparison of $S = 0$ and $S = \frac{1}{2}$ impurities in the Haldane chain compound Y_2BaNiO_5* , Phys. Rev. B **69** (2004), no. 14, 144404. 58

[ESAA07] Sebastian Eggert, Olav F. Syljuåsen, Fabrizio Anfuso, and Markus Andres, *Universal Alternating Order around Impurities in Antiferromagnets*, Phys. Rev. Lett. **99** (2007), no. 9, 097204. 58

[HKP+99] M. Hücker, V. Kataev, J. Pommer, J. Harraß, A. Hosni, C. Pflitsch, R. Gross, and B. Büchner, *Mobility of holes and suppression of antiferromagnetic order in $La_{2-x}Sr_xCuO_4$* , Phys. Rev. B **59** (1999), no. 2, R725–R728. 33

[HN96] Koji Hukushima and Koji Nemoto, *Exchange Monte Carlo Method and Application to Spin Glass Simulations*, Journal of the Physical Society of Japan **65** (1996), no. 6, 1604–1608. 13

[HS00] Patrik Henelius and Anders W. Sandvik, *Sign problem in Monte Carlo simulations of frustrated quantum spin systems*, Phys. Rev. B **62** (2000), no. 2, 1102–1113. 13

[HSS07a] Kaj H. Höglund, Anders W. Sandvik, and Subir Sachdev, *Impurity Induced Spin Texture in Quantum Critical 2D Antiferromagnets*, Phys. Rev. Lett. **98** (2007), no. 8, 087203. 14, 58

[HSS07b] _____, *Impurity Induced Spin Texture in Quantum Critical 2D Antiferromagnets*, Phys. Rev. Lett. **98** (2007), no. 8, 087203. 59, 60, 61, 62, 64

[IFT98] Masatoshi Imada, Atsushi Fujimori, and Yoshinori Tokura, *Metal-insulator transitions*, Rev. Mod. Phys. **70** (1998), no. 4, 1039–1263. 9

[JFHac+00] M.-H. Julien, T. Fehér, M. Horvatić, C. Berthier, O. N. Bakharev, P. Ségransan, G. Collin, and J.-F. Marucco, *^{63}Cu NMR Evidence for Enhanced Antiferromagnetic Correlations around Zn Impurities in $YBa_2Cu_3O_{6.7}$*, Phys. Rev. Lett. **84** (2000), no. 15, 3422–3425. 58

[JNCW08] F-J Jiang, M Nyfeler, S Chandrasekharan, and U-J Wiese, *From an antiferromagnet to a valence bond solid: evidence for a first-order phase transition*, Journal of Statistical Mechanics: Theory and Experiment **2008** (2008), no. 02, P02009. 39, 44, 45

[KBB+92] B. Keimer, N. Belk, R. J. Birgeneau, A. Cassanho, C. Y. Chen, M. Greven, M. A. Kastner, A. Aharony, Y. Endoh, R. W. Erwin, and G. Shirane, *Magnetic excitations in pure, lightly doped, and weakly metallic La_2CuO_4*, Phys. Rev. B **46** (1992), no. 21, 14034–14053. 33

[KMMS08] Ribhu K. Kaul, Roger G. Melko, Max A. Metlitski, and Subir Sachdev, *Imaging Bond Order near Nonmagnetic Impurities in Square-Lattice Antiferromagnets*, Phys. Rev. Lett. **101** (2008), no. 18, 187206. 58

[KMP+08] A. B. Kuklov, M. Matsumoto, N. V. Prokof'ev, B. V. Svistunov, and M. Troyer, *Deconfined Criticality: Generic First-Order Transition in the SU(2) Symmetry Case*, Phys. Rev. Lett. **101** (2008), no. 5, 050405. 39, 45

[KT07] Naoki Kawashima and Yuta Tanabe, *Ground States of the $SU(N)$ Heisenberg Model*, Phys. Rev. Lett. **98** (2007), no. 5, 057202. 69

[KTH+00] K. Kato, S. Todo, K. Harada, N. Kawashima, S. Miyashita, and H. Takayama, *Quantum Phase Transition of the Randomly Diluted Heisenberg Antiferromagnet on a Square Lattice*, Phys. Rev. Lett. **84** (2000), no. 18, 4204–4207. 33

[LS04] Michael Levin and T. Senthil, *Deconfined quantum criticality and Néel order via dimer disorder*, Phys. Rev. B **70** (2004), no. 22, 220403. 42, 47, 49

[LSK09] Jie Lou, Anders W. Sandvik, and Naoki Kawashima, *Antiferromagnetic to valence-bond-solid transitions in two-dimensional $SU(N)$ Heisenberg models with multispin interactions*, Phys. Rev. B **80** (2009), no. 18, 180414. 39, 44, 57, 64, 70, 72

[MACM94] A. V. Mahajan, H. Alloul, G. Collin, and J. F. Marucco, *^{89}Y NMR probe of Zn induced local moments in $YBa_2(Cu_{1-y}Zn_y)_3O_{6+x}$*, Phys. Rev. Lett. **72** (1994), no. 19, 3100–3103. 58

[Man91] Efstratios Manousakis, *The spin-half Heisenberg antiferromagnet on a square lattice and its application to the cuprous oxides*, Rev. Mod. Phys. **63** (1991), no. 1, 1–62. 10, 11

[MK08] Roger G. Melko and Ribhu K. Kaul, *Scaling in the Fan of an Unconventional Quantum Critical Point*, Phys. Rev. Lett. **100** (2008), no. 1, 017203. 39, 44, 64

[MLRD97] George Balster Martins, Markus Laukamp, José Riera, and Elbio Dagotto, *Local Enhancement of Antiferromagnetic Correlations by Nonmagnetic Impurities*, Phys. Rev. Lett. **78** (1997), no. 18, 3563–3566. 58

[MS08] Max A. Metlitski and Subir Sachdev, *Edge and impurity response in two-dimensional quantum antiferromagnets*, Phys. Rev. B **78** (2008), no. 17, 174410. 35, 37

[MV08] O. I. Motrunich and A. Vishwanath, *Comparative study of Higgs transition in one-component and two-component lattice superconductor models*, ArXiv e-prints (2008). 39, 45

[OTI+99] S. Ohsugi, Y. Tokunaga, K. Ishida, Y. Kitaoka, M. Azuma, Y. Fujishiro, and M. Takano, *Impurity-induced staggered polarization and antiferromagnetic order in spin-$\frac{1}{2}$ Heisenberg two-leg ladder compound $SrCu_2O_3$: Extensive Cu NMR and NQR studies*, Phys. Rev. B **60** (1999), no. 6, 4181–4190. 58

[PST98a] N. V. Prokof'ev, B. V. Svistunov, and I. S. Tupitsyn, *Exact, Complete, and Universal Continuous-Time Worldline Monte Carlo Approach to the Statistics of Discrete Quantum Systems*, Sov. Phys. - JETP **87** (1998), 310. 12

[PST98b] _____, *"Worm" algorithm in quantum Monte Carlo simulations*, Physics Letters A **238** (1998), no. 4-5, 253 – 257. 12

[PSV01] Anatoli Polkovnikov, Subir Sachdev, and Matthias Vojta, *Impurity in a d-Wave Superconductor: Kondo Effect and STM Spectra*, Phys. Rev. Lett. **86** (2001), no. 2, 296–299. 58

[RS89] N. Read and Subir Sachdev, *Valence-bond and spin-Peierls ground states of low-dimensional quantum antiferromagnets*, Phys. Rev. Lett. **62** (1989), no. 14, 1694–1697. 69

[RY88] J. D. Reger and A. P. Young, *Monte Carlo simulations of the spin-1/2 Heisenberg antiferromagnet on a square lattice*, Phys. Rev. B **37** (1988), no. 10, 5978–5981. 10

[Sac01] S. Sachdev, *Quantum phase transitions*, first paperback ed., Cambridge, New York, 2001. 36

[San99] Anders W. Sandvik, *Stochastic series expansion method with operator-loop update*, Phys. Rev. B **59** (1999), no. 22, R14157–R14160. 12

[San02] _____, *Classical percolation transition in the diluted two-dimensional $S = \frac{1}{2}$ Heisenberg antiferromagnet*, Phys. Rev. B **66** (2002), no. 2, 024418. 33

[San05] _____, *Ground State Projection of Quantum Spin Systems in the Valence-Bond Basis*, Phys. Rev. Lett. **95** (2005), no. 20, 207203. 14, 17, 18, 24, 27

[San07] _____, *Evidence for Deconfined Quantum Criticality in a Two-Dimensional Heisenberg Model with Four-Spin Interactions*, Phys. Rev. Lett. **98** (2007), no. 22, 227202. 39, 43, 48, 57, 75

[San10] _____, *Continuous Quantum Phase Transition between an Antiferromagnet and a Valence-Bond Solid in Two Dimensions: Evidence for Logarithmic Corrections to Scaling*, Phys. Rev. Lett. **104** (2010), no. 17, 177201. 39, 49, 53, 66, 68

[SBS+04] T. Senthil, Leon Balents, Subir Sachdev, Ashvin Vishwanath, and Matthew P. A. Fisher, *Quantum criticality beyond the Landau-Ginzburg-Wilson paradigm*, Phys. Rev. B **70** (2004), no. 14, 144407. 39, 42, 67

[SBV99] Subir Sachdev, Chiranjeeb Buragohain, and Matthias Vojta, *Quantum Impurity in a Nearly Critical Two-Dimensional Antiferromagnet*, Science **286** (1999), no. 5449, 2479–2482. 58

[SDSS02] A. W. Sandvik, S. Daul, R. R. P. Singh, and D. J. Scalapino, *Striped phase in a quantum xy model with ring exchange*, Phys. Rev. Lett. **89** (2002), 247201. 42

[SE10] Anders W. Sandvik and Hans Gerd Evertz, *Loop updates for variational and projector quantum Monte Carlo simulations in the valence-bond basis*, Phys. Rev. B **82** (2010), no. 2, 024407. 14, 17, 19, 22, 24, 27, 29

[SM06] A.W. Sandvik and R.G. Melko, *Ground-state phases and quantum phase transitions in a two-dimensional spin-1/2 xy model with four-spin interactions*, Annals of Physics **321** (2006), no. 7, 1651 – 1668, <ce:title>July 2006 Special Issue</ce:title>. 42

[SS10] A. Sen and A. W. Sandvik, *Example of a first-order N\'eel to Valence-Bond-Solid transition in two-dimensions*, ArXiv e-prints (2010). 48, 52, 53

[SVB+04] T. Senthil, Ashvin Vishwanath, Leon Balents, Subir Sachdev, and Matthew P. A. Fisher, *Deconfined Quantum Critical Points*, Science **303** (2004), no. 5663, 1490–1494. 39, 42

[TMEU97] Masashi Takigawa, Naoki Motoyama, Hiroshi Eisaki, and Shinichi Uchida, *Field-induced staggered magnetization near impurities in the S= one-dimensional Heisenberg antiferromagnet* Sr_2CuO_3 , Phys. Rev. B **55** (1997), no. 21, 14129–14132. 58

[TSHac99] F. Tedoldi, R. Santachiara, and M. Horvatić, ^{89}Y *NMR Imaging of the Staggered Magnetization in the Doped Haldane Chain* $Y_2BaNi_{1-x}Mg_xO_5$, Phys. Rev. Lett. **83** (1999), no. 2, 412–415. 14, 15, 58

[VMG+02] O. P. Vajk, P. K. Mang, M. Greven, P. M. Gehring, and J. W. Lynn, *Quantum Impurities in the Two-Dimensional Spin One-Half Heisenberg Antiferromagnet*, Science **295** (2002), no. 5560, 1691–1695. 17, 33

[WJ09] Sandro Wenzel and Wolfhard Janke, *Comprehensive quantum Monte Carlo study of the quantum critical points in planar dimerized/quadrumerized Heisenberg models*, Phys. Rev. B **79** (2009), no. 1, 014410. 61

[WS10] Ling Wang and Anders W. Sandvik, *Low-energy excitations of two-dimensional diluted Heisenberg quantum antiferromagnets*, Phys. Rev. B **81** (2010), no. 5, 054417. 33

[ZGW+10] Wanzhou Zhang, Wenan Guo, Ling Wang, Kaj H. Höglund, and Anders W. Sandvik, *Effects of edge disorder in nanoscale antiferromagnetic clusters*, Phys. Rev. B **82** (2010), no. 1, 012401. 33